Research Article | Vol. 32, No. 13 / 17 Jun 2024 / Optics Express 23347
Optics EXPRESS

Tunable wave localization at the Dirac frequency in a metallic photonic crystal cavity

LEI HU,[1,2,†] ERLEI WANG,[3,†] JIANGYING XIA,[1,2,7,†] WENYU DU,[2] GUANGYIN QU,[2] YUE WANG,[4] SIQI LI,[1,2] FENG XU,[2] YU LIU,[1,2] BENLI YU,[1,2] KANG XIE,[5] JUNXI ZHANG,[6] AND ZHIJIA HU[1,2,8]

[1]*Information Materials and Intelligent Sensing Laboratory of Anhui Province, School of Materials Science and Engineering, Anhui University, Hefei 230601, China*
[2]*Key Laboratory of Opto-Electronic Information Acquisition and Manipulation of Ministry of Education, School of Physics and Optoelectronic Engineering, Anhui University, Hefei 230601, China*
[3]*School of Mechanical and Electrical Engineering, Zhoukou Normal University, Zhoukou 466000, China*
[4]*School of Computer Science and Technology, Anhui University of Technology, Maanshan 243032, China*
[5]*School of Opto-Electronic Engineering, Zaozhuang University, Zaozhuang 277160, China*
[6]*Anhui Province Key Laboratory of Measuring Theory and Precision Instrument, School of Instrument Science and Opto-electronics Engineering, Hefei University of Technology, Hefei 230009, China*
[7]*xjy@ahu.edu.cn*
[8]*zhijiahu@ahu.edu.cn*
[†]These authors contributed equally to this work.

Abstract: In this study, the two-dimensional (2D) triangular lattice metallic photonic crystals (PCs) in visible and infrared bands have been utilized to achieve light confinement at the Dirac frequency. Distinct from the traditional bandgap or total internal reflection cavity modes, the unique photonic localization mechanism leads to an unusual algebraic decay of state and a unique frequency located beyond any bandgaps. This investigation delves into the band structure analysis of 2D metallic PCs, specifically focusing on their distinctive features, such as photonic bandgaps and Dirac cones. The plane wave expansion (PWE) method, enhanced with a linearization technique, is employed for band structure calculations, considering both the frequency-dependent dielectric properties and the intrinsic lossy nature of metallic materials described by the Drude model. The study provides a comprehensive derivation of the PWE equations for metallic PCs and investigates their band characteristics under both TM and TE polarizations. Focusing on TM modes in triangular lattice metallic PCs, it reveals zero density of states (DOS) at K points of the Brillouin corner and the existence of Dirac cones with linearly dispersion and linearly vanishing DOS. The study extends to exploring localized modes at Dirac frequencies, employing a relativistic quantum mechanics approach analogous to graphene's charge carriers. Theoretical predictions are corroborated by numerical simulations, and the potential for tunable Dirac localized modes is highlighted. This research not only deepens the understanding of Dirac properties in graphene-like systems but also lays the groundwork for further exploration of the practical quasi-2D devices, which will provide assistance in the integration of micro- and nano-devices, especially in applications requiring long-range coupling, given the critical importance of optical cavities in contemporary optical technologies.

© 2024 Optica Publishing Group under the terms of the Optica Open Access Publishing Agreement

1. Introduction

Since A. Geim and K. Novoselov [1] successfully isolated the two-dimensional (2D) graphene, 2D materials have attracted widespread attention from researchers for their fascinating properties. One of the most intriguing features of 2D materials is the Dirac cone in their electronic band structure.

#525384 https://doi.org/10.1364/OE.525384
Journal © 2024 Received 12 Apr 2024; revised 23 May 2024; accepted 1 Jun 2024; published 11 Jun 2024

Optics EXPRESS

The Dirac cone is a prominent feature in the band structures of 2D materials and has played a crucial role in understanding the unconventional electronic transport properties of graphene [2] and similar 2D topological insulators [3]. In these systems, electronic transport within the Dirac cones mirrors the behavior of massless Fermions. Close to the Fermi level, the energy bands of these materials intersect in a conical shape, reflecting the massless Dirac equation in the energy-momentum relationship [4], characterized by linear dispersion and convergence at the Dirac point. Research has revealed that 2D materials with Dirac cones exhibit a variety of unique physical properties, including diverse quantum Hall effects [5] and exceptional carrier mobility [6]. Furthermore, as investigated by A. H. Castro Neto et al. [7], the introduction of point defects into the graphene lattice results in localized electronic states characterized by a $1/r$ decay in the wave function near the defect, underlining the intricate electron behavior in these systems.

The analogy between massless fermions and photons has led to the introduction of the concept of Dirac cones into photonic crystal (PC) research, especially in 2D triangular series lattice structures [8–10]. While initial research focused on bandgap generation [11], the later recognition of unique dispersion properties at the Brillouin zone corners in these structures [12,13] has expanded the understanding of Dirac points in PCs. These PC structures, mirroring their electronic counterparts, feature unique density of states (DOS) and dispersion relationships that linearly vary near the Dirac points [14,15]. A range of intriguing Dirac relativistic wave transport phenomena, including electromagnetic topological edge states [16], Klein tunneling [17], Zitterbewegung [18], and pseudo-diffusion [19,20], have been replicated in 2D PCs.

Meanwhile, the discovery of in-cavity light localization near Dirac points in PCs by K. Xie et al. [21] overturned the prevailing belief that 2D localized modes at Dirac frequencies were unachievable without a complete photonic bandgap. This breakthrough, not reliant on bandgap or total internal reflection mechanisms, has profound implications for optical device design, leveraging Dirac points in photonic band structures to effectively suppress radiation loss. It also led to the emergence of algebraic decay localized modes, enhancing long-range coupling in PC devices and influencing the design of advanced filters and lasers. Subsequent studies have entered into new realms of 2D localized modes in various PC lattices [22,23], exploring spatial algebraic solitons in nonlinear lattices [24], guided modes in PC fibers [25], and validated through microwave experiment [26], particularly near the Dirac frequency. These researches have unveiled algebraic decay of states and unique frequency behaviors beyond bandgaps, yet was primarily limited to conventional dielectric materials, without incorporating materials like metals with dispersive properties, limiting the theory's breadth.

In recent years, extensive researches have explored the properties of Dirac cones in metallic materials, specifically in various lattice structures such as triangular and honeycomb lattices. These researches, encompassing either theoretical or experimental approaches, has investigated phenomena like electromagnetic beam propagation [27,28], properties of the eigenstates of the Dirac billiard [29,30], localized edge states [31,32], biosensors [33], high transmission properties [34], and has contributed to the development of continuous quantum wave search algorithms [35]. However, most of these studies have been conducted in the microwave regime. Investigations into metallic PC Dirac cones in the visible and near-infrared spectra are still in development stages, with metal-based PC cavity localized modes at the Dirac frequency remaining unreported. Our study here focuses on the relatively unexplored area of metallic PCs, examining tunable wave localization mechanisms at the Dirac point. These structures, characterized by the incorporation of metallic materials, display complex dielectric constants with frequency-dependent dispersion and absorption characteristics. This research not only broadens the scientific understanding of metallic PCs but also opens up new possibilities for tunable wave localization at the Dirac point, a field ripe for further exploration.

Optics EXPRESS

2. Band structure of 2D metallic photonic crystal

The distinctive features of metallic PCs, including photonic bandgaps and Dirac cones, are crucial to their unique properties. A thorough understanding of their band structure is essential for further exploration. For non-dispersive PCs, the plane wave expansion (PWE) method [36] emerges as a valuable tool for calculating the band structure. V. Kuzmiak et al. [37] introduced an improved linearization method for nonlinear equations within the traditional PWE framework, thus broadening its applicability to dispersion models. This advancement enables the PWE method to be equally effective across various scenarios. Given that the PWE method enhances the physical understanding of PCs, we begin the process by deriving the general form of the PWE equation for metallic PCs. This foundational step establishes a basis for a more profound exploration of their unique properties.

2.1. Band structure calculation of 2D metallic photonic crystals: linearization plane wave expansion method

In the visible and near-infrared range (100 THz ~ 900 THz), the dielectric constant of metallic materials demonstrates frequency dependence. It is, therefore, essential to employ the dielectric function $\varepsilon(\omega)$ to characterize their frequency-dependent dielectric properties. When subjected to an external electromagnetic field, the internal electrons of a metal can move freely, forming a "metal electron gas" and exhibiting electromagnetic properties akin to those of plasma. In the realm of electromagnetics, metals can be conceptualized as a form of "solid plasma". The commonly employed method to describe the dielectric function of metal/plasma is the free electron gas model, widely referred to as the Drude model:

$$\varepsilon(\omega) = 1 - \frac{\omega_p^2}{\omega^2 + i\omega\omega_\tau} \tag{1}$$

where the real and imaginary parts of the dielectric function are:

$$\begin{aligned} \varepsilon_1(\omega) &= 1 - \frac{\omega_p^2}{\omega^2+\omega_\tau^2} \\ \varepsilon_2(\omega) &= \frac{\omega_p^2\omega_\tau}{\omega^3+\omega\omega_\tau^2} \end{aligned} \tag{2}$$

Here, ω represents the incident wave frequency, ω_p denotes the plasma frequency of the electron gas, and ω_τ is the damping frequency. The specific values of ω_p and ω_τ can be ascertained through fitting to experimental data [38], with the ω_p and ω_τ values for some frequently encountered metals being: 3570/19.4 THz (Al), 1914/8.34 THz (Cu), 2175/6.5 THz (Au), and 2175/4.35 THz (Ag) [39].

In Table 1, the cross-sectional schematic diagram on the *xy* plane depicts a 2D metallic PC consisting of metallic cylinders arranged within a metal/plasma background, structured according to a specific lattice (square/triangular) arrangement. Adhering to a common assumption in 2D PC calculations [36,37], it is considered that the metallic cylinders are aligned parallel to the *z*-axis and do not overlap. The lattice constant is denoted as a, and the cylinder's radius is represented as r_a. The relative dielectric functions of the cylinders and background are characterized as follows:

$$\begin{aligned} \varepsilon_a(\omega) &= 1 - \frac{\omega_{pa}^2}{\omega^2+i\omega\omega_{\tau a}} \\ \varepsilon_b(\omega) &= 1 - \frac{\omega_{pb}^2}{\omega^2+i\omega\omega_{\tau b}} \end{aligned} \tag{3}$$

The intersections of the axes of these rods with the *xy* plane form a 2D Bravais lattice, with lattice sites defined by the translation vector $\mathbf{R} = m_1\mathbf{a}_1 + m_2\mathbf{a}_2$; here, $\mathbf{a}_1$ and $\mathbf{a}_2$ are the two noncollinear primitive translation vectors of the lattice, while m_1 and m_2 are arbitrary integers.

Optics EXPRESS

Table 1. Lattice information for the metallic photonic crystal

Lattice Type	Lattice Diagram	Reciprocal Lattice	Lattice basis vectors	Reciprocal basis vectors
Square	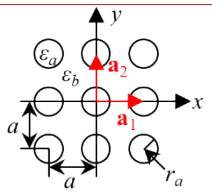	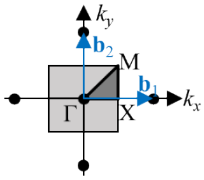	$\mathbf{a}_1 = a(1,0)$ $\mathbf{a}_2 = a(0,1)$	$\mathbf{b}_1 = \frac{2\pi}{a}(1,0)$ $\mathbf{b}_2 = \frac{2\pi}{a}(0,1)$
Triangular	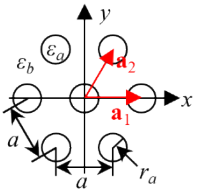	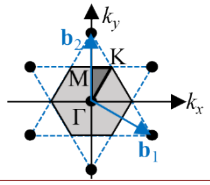	$\mathbf{a}_1 = a(1,0)$ $\mathbf{a}_2 = a\left(\frac{1}{2}, \frac{\sqrt{3}}{2}\right)$	$\mathbf{b}_1 = \frac{2\pi}{a}\left(1, -\frac{\sqrt{3}}{3}\right)$ $\mathbf{b}_2 = \frac{2\pi}{a}\left(0, \frac{2\sqrt{3}}{3}\right)$

Utilizing the periodic characteristics of 2D PCs, the distribution of the dielectric function across the entire transverse plane is governed by the equation:

$$\varepsilon(\mathbf{r}_{\parallel}) = \varepsilon_b(\omega) + [\varepsilon_a(\omega) - \varepsilon_b(\omega)] \sum_{m_1, m_2 \in Z} S(\mathbf{r}_{\parallel} - \mathbf{R}) \tag{4}$$

Here, $\mathbf{r}_{||}$ represents the transverse plane position vector and the S function is defined as:

$$S(\mathbf{r}_{\parallel} - \mathbf{R}) = \begin{cases} 1, & |\mathbf{r}_{\parallel} - \mathbf{R}| \le r_a \\ 0, & |\mathbf{r}_{\parallel} - \mathbf{R}| > r_a \end{cases} \tag{5}$$

We will now proceed to derive the PWE eigenequation for this 2D metallic PC and to analyze its band structure properties.

(1) TM polarization

By modifying the Helmholtz equation (Eq. (12) of Ref. [36]) for TM polarization (characterized by $E_x = E_y = H_z = 0$, with H_x, H_y and E_z being nonzero) within a 2D PC, the following expression is derived:

$$\left(\frac{\partial^2}{\partial x^2} + \frac{\partial^2}{\partial y^2}\right) E_z(\mathbf{r}_{\parallel}) = -\varepsilon(\mathbf{r}_{\parallel}) \frac{\omega^2}{c^2} E_z(\mathbf{r}_{\parallel}) \tag{6}$$

The dielectric function $\varepsilon(\mathbf{r}_{||})$ and the electric field $E_z(\mathbf{r}_{||})$ can be expanded into Fourier series within the reciprocal space:

$$\begin{aligned} \varepsilon(\mathbf{r}_{\parallel}) &= \sum_{\mathbf{G}_{\parallel}} \kappa(\mathbf{G}_{\parallel}) \exp(i\mathbf{G}_{\parallel} \cdot \mathbf{r}_{\parallel}) \\ E_z(\mathbf{r}_{\parallel}) &= E_{z,\mathbf{k}_{\parallel},n}(\mathbf{r}_{\parallel}) = \sum_{\mathbf{G}_{\parallel}} E'_{z,\mathbf{k}_{\parallel},n}(\mathbf{G}_{\parallel}) \exp[i(\mathbf{k}_{\parallel} + \mathbf{G}_{\parallel}) \cdot \mathbf{r}_{\parallel}] \end{aligned} \tag{7}$$

where $\mathbf{G}_{||} = l_1\mathbf{b}_1 + l_2\mathbf{b}_2$ ($\mathbf{b}_1$ and $\mathbf{b}_2$ are 2D primitive translation vectors of the reciprocal lattice satisfying $\mathbf{a}_i \cdot \mathbf{b}_j = 2\pi\delta_{ij}$ for $i,j = 1,2$, l_1 and l_2 are arbitrary integers) represents the reciprocal lattice vector, $\mathbf{k}_{||}$ is the wave vector within the first Brillouin zone, while $\kappa(\mathbf{G}_{||})$ and $E'_{z,\mathbf{k}_{||},n}(\mathbf{G}_{||})$ are the Fourier expansion coefficients of $\varepsilon(\mathbf{r}_{||})$ and $E_z(\mathbf{r}_{||})$, respectively. Substituting Eq. (7) into Eq. (6) results in the eigenequation for the Fourier expansion coefficient set $\{E'_{z,\mathbf{k}_{||},n}(\mathbf{G}_{||})\}$ of the

Optics EXPRESS

electric field:

$$|\mathbf{k}_{\|}+\mathbf{G}_{\|}|^2 E_{z,\mathbf{k}_{\|},n}(\mathbf{G}_{\|}) = \frac{\omega^2}{c^2}\sum_{\mathbf{G}'_{\|}}\kappa(\mathbf{G}_{\|}-\mathbf{G}'_{\|})E_{z,\mathbf{k}_{\|},n}(\mathbf{G}'_{\|}) = \frac{\omega^2}{c^2}\kappa(0)E_{z,\mathbf{k}_{\|},n}(\mathbf{G}_{\|}) + \frac{\omega^2}{c^2}\sum_{\mathbf{G}'_{\|},\mathbf{G}'_{\|}\neq\mathbf{G}_{\|}}\kappa(\mathbf{G}_{\|}-\mathbf{G}'_{\|})E_{z,\mathbf{k}_{\|},n}(\mathbf{G}'_{\|}) \tag{8}$$

where the prime on $E'_{z,\mathbf{k}_{||},n}(\mathbf{G}_{||})$ is omitted for clarity. According to Eqs. (19–21) in Ref. [36], the Fourier expansion coefficient of $\varepsilon(\mathbf{r}_{||})$ is expressed as:

$$\kappa(\mathbf{G}_{\|}) = \begin{cases} 1-\frac{\omega_{pb}^2}{\omega^2+i\omega\omega_{\tau b}}+\left(\frac{\omega_{pb}^2}{\omega^2+i\omega\omega_{\tau b}}-\frac{\omega_{pa}^2}{\omega^2+i\omega\omega_{\tau a}}\right)f, & \mathbf{G}_{\|}=0 \\ 2f\left(\frac{\omega_{pb}^2}{\omega^2+i\omega\omega_{\tau b}}-\frac{\omega_{pa}^2}{\omega^2+i\omega\omega_{\tau a}}\right)\frac{J_1(G_{\|}r_a)}{G_{\|}r_a}, & \mathbf{G}_{\|}\neq 0 \end{cases} \tag{9}$$

where $G=|\mathbf{G}|$, $a_c=|\mathbf{a}_1\times\mathbf{a}_2|$ is the area of the primitive unit cell, $f=\pi {r_a}^2/a_c$ is the filling ratio of the metallic PC, representing the ratio of the area of the cylinder to the area of the unit cell, and $J_1(x)$ represents a first-order Bessel function.

For calculation convenience, let $\omega=\theta c$, $\omega_{pa}=\eta_a c$, $\omega_{pb}=\eta_b c$, $\omega_{\tau a}=\mu_a c$, $\omega_{\tau b}=\mu_b c$, $I(\mathbf{G}_{||})=2fJ_1(\mathbf{G}_{||}r_a)/(\mathbf{G}_{||}r_a)$, with c being the speed of light in vacuum, and then substitute Eq. (9) into Eq. (8). Subsequently, we obtain:

$$\sum_{\mathbf{G}'_{\|}}\left\{\left[|\mathbf{k}_{\|}+\mathbf{G}_{\|}|^2-\theta^2+\frac{\theta^2\eta_b^2}{\theta^2+i\theta\mu_b}+\left(\frac{\theta^2\eta_a^2}{\theta^2+i\theta\mu_a}-\frac{\theta^2\eta_b^2}{\theta^2+i\theta\mu_b}\right)f\right]\delta(\mathbf{G}_{\|}-\mathbf{G}'_{\|}) + \left(\frac{\theta^2\eta_a^2}{\theta^2+i\theta\mu_a}-\frac{\theta^2\eta_b^2}{\theta^2+i\theta\mu_b}\right)I(\mathbf{G}_{\|}-\mathbf{G}'_{\|})\right\}E_{z,\mathbf{k}_{\|},n}(\mathbf{G}'_{\|})=0 \tag{10}$$

Introduce five $NG\times NG$ matrices, where NG is the number of plane waves utilized in Eq. (7):

$$\begin{aligned} \mathbf{A}_{\mathbf{G}_{\|},\mathbf{G}'_{\|}} &= \delta(\mathbf{G}_{\|}-\mathbf{G}'_{\|}) \\ \mathbf{B}_{\mathbf{G}_{\|},\mathbf{G}'_{\|}} &= i(\mu_a+\mu_b)\delta(\mathbf{G}_{\|}-\mathbf{G}'_{\|}) \\ \mathbf{C}_{\mathbf{G}_{\|},\mathbf{G}'_{\|}} &= [|\mathbf{k}_{\|}+\mathbf{G}_{\|}|^2+\mu_a\mu_b+\eta_b^2(1-f)+\eta_a^2 f]\delta(\mathbf{G}_{\|}-\mathbf{G}'_{\|}) \\ &\quad +(\eta_a^2-\eta_b^2)I(\mathbf{G}_{\|}-\mathbf{G}'_{\|}) \\ \mathbf{D}_{\mathbf{G}_{\|},\mathbf{G}'_{\|}} &= i[(\mu_a+\mu_b)|\mathbf{k}_{\|}+\mathbf{G}_{\|}|^2+\eta_b^2\mu_a(1-f)+\eta_a^2\mu_b f]\delta(\mathbf{G}_{\|}-\mathbf{G}'_{\|}) \\ &\quad +i(\eta_a^2\mu_b-\eta_b^2\mu_a)I(\mathbf{G}_{\|}-\mathbf{G}'_{\|}) \\ \mathbf{E}_{\mathbf{G}_{\|},\mathbf{G}'_{\|}} &= \mu_a\mu_b|\mathbf{k}_{\|}+\mathbf{G}_{\|}|^2\delta(\mathbf{G}_{\|}-\mathbf{G}'_{\|}) \end{aligned} \tag{11}$$

By eliminating the denominator from Eq. (10), Eq. (11) is reduced to a fourth-order nonlinear eigenequation:

$$(\theta^4\mathbf{A}+\theta^3\mathbf{B}-\theta^2\mathbf{C}-\theta\mathbf{D}+\mathbf{E})E_z=0 \tag{12}$$

where E_z is a column vector $\{E_{z,\mathbf{k}_{||},n}(\mathbf{G}'_{||})\}$. By applying a linear transformation to Eq. (12), it is transformed into a $4\,NG\times 4\,NG$ matrix equation:

$$\begin{pmatrix} \mathbf{O} & \mathbf{I} & \mathbf{O} & \mathbf{O} \\ \mathbf{O} & \mathbf{O} & \mathbf{I} & \mathbf{O} \\ \mathbf{O} & \mathbf{O} & \mathbf{O} & \mathbf{I} \\ -\mathbf{A}^{-1}\mathbf{E} & \mathbf{A}^{-1}\mathbf{D} & \mathbf{A}^{-1}\mathbf{C} & -\mathbf{A}^{-1}\mathbf{B} \end{pmatrix}\begin{pmatrix} E_z \\ \theta E_z \\ \theta^2 E_z \\ \theta^3 E_z \end{pmatrix} = \theta\begin{pmatrix} E_z \\ \theta E_z \\ \theta^2 E_z \\ \theta^3 E_z \end{pmatrix} \tag{13}$$

In the preceding equation, $\mathbf{O}$ and $\mathbf{I}$ represent respectively the zero matrix and identity matrix, both having dimensions $NG\times NG$. Using this representation, the eigenvalue problem for TM

Optics EXPRESS

waves in the metallic PC translates into solving for the eigenvalue θ in Eq. (13), thereby enabling the calculation of the eigenfrequency as $\omega = \theta c$. It is important to note that, in contrast to the typical PWE method, the operator matrix obtained through the linearized PWE method is not Hermitian. Consequently, its eigenvalues might include complex numbers, where the imaginary part indicates the loss of electromagnetic waves. In the case of actual lossy dispersion media, eigen solutions possessing both positive real and negative imaginary parts are physically significant. Therefore, it is necessary to select eigenvalues that meet these conditions and utilize their real parts to determine the final band structure.

The presence of $\omega_{\tau a}$ and $\omega_{\tau b}$ introduces loss in electromagnetic waves. However, they have minimal impact on solving the eigenvalues. When the damping frequency, namely, $\omega_{\tau a} = \omega_{\tau b} = 0$, is excluded from consideration, the equations can undergo significant simplification. Under these conditions, with $\mu_a = \mu_b = 0$, matrices $\mathbf{B}$, $\mathbf{D}$ and $\mathbf{E}$ all become the zero matrix $\mathbf{O}$, and the matrix equation simplifies to $\mathbf{A}^{-1}\mathbf{C}E_z = \theta^2 E_z$. The operator matrix thus transforms from $4\,NG \times 4\,NG$ to $NG \times NG$, leading to an approximate 16-fold increase in calculation efficiency.

If the background constitutes air, namely $\omega_{pb} = \omega_{\tau b} = 0$, the eigenequation can be simplified by substituting $\eta_b = \mu_b = 0$ into Eq. (11). Specifically, when excluding the loss of the metal columns ($\mu_a = 0$), the eigenequation can be further simplified to:

$$\sum_{\mathbf{G'}_\parallel} \left[\left(|\mathbf{k}_\parallel + \mathbf{G}_\parallel|^2 + \frac{\omega_{pa}^2}{c^2} f \right) \delta(\mathbf{G}_\parallel - \mathbf{G'}_\parallel) + \frac{\omega_{pa}^2}{c^2} I(\mathbf{G}_\parallel - \mathbf{G'}_\parallel) \right] E_z = \frac{\omega^2}{c^2} E_z \tag{14}$$

which corresponds precisely to Eq. (2.6) in Ref. [37].

(2) TE polarization

The eigenvalue equation for TE polarization (characterized by $H_x = H_y = E_z = 0$, with E_x, E_y and H_z being nonzero) in a 2D PC, as delineated in Eq. (9) of Ref. [36], is equivalently represented as:

$$\begin{aligned} &\sum_{\mathbf{G'}_\parallel, \mathbf{G'}_\parallel \neq \mathbf{G}_\parallel} \chi(\mathbf{G}_\parallel - \mathbf{G'}_\parallel)(\mathbf{k}_\parallel + \mathbf{G}_\parallel) \cdot (\mathbf{k}_\parallel + \mathbf{G'}_\parallel) H_{z,\mathbf{k}_\parallel,n}(\mathbf{G'}_\parallel) \\ &+\chi(0)|\mathbf{k}_\parallel + \mathbf{G}_\parallel|^2 H_{z,\mathbf{k}_\parallel,n}(\mathbf{G}_\parallel) = \frac{\omega^2}{c^2} H_{z,\mathbf{k}_\parallel,n}(\mathbf{G}_\parallel) \end{aligned} \tag{15}$$

The quantities $\chi(\mathbf{G}_{||})$ and $H_{z,\mathbf{k}_{||},n}(\mathbf{G}_{||})$ correspond to the reciprocal of the dielectric function $1/\varepsilon(\mathbf{r}_{||})$ and the Fourier expansion coefficients of the magnetic field $H_z(\mathbf{r}_{||})$, respectively. Analogous to Eq. (9), the Fourier expansion coefficient of $1/\varepsilon(\mathbf{r}_{||})$ is expressed as:

$$\chi(\mathbf{G}_\parallel) = \begin{cases} \frac{(\omega^2 + i\omega\omega_{\tau b})(1-f)}{\omega^2 - \omega_{pb}^2 + i\omega\omega_{\tau b}} + \frac{(\omega^2 + i\omega\omega_{\tau a})f}{\omega^2 - \omega_{pa}^2 + i\omega\omega_{\tau a}}, & \mathbf{G}_\parallel = 0 \\ 2f \left(\frac{\omega^2 + i\omega\omega_{\tau a}}{\omega^2 - \omega_{pa}^2 + i\omega\omega_{\tau a}} - \frac{\omega^2 + i\omega\omega_{\tau b}}{\omega^2 - \omega_{pa}^2 + i\omega\omega_{\tau b}} \right) \frac{J_1(G_\parallel r_a)}{G_\parallel r_a}, & \mathbf{G}_\parallel \neq 0 \end{cases} \tag{16}$$

Upon substituting Eq. (16) into Eq. (15), the result is:

$$\left(\frac{\omega^2 + i\omega\omega_{\tau b}}{\omega^2 - \omega_{pb}^2 + i\omega\omega_{\tau b}} \mathbf{M} + \frac{\omega^2 + i\omega\omega_{\tau a}}{\omega^2 - \omega_{pa}^2 + i\omega\omega_{\tau a}} \mathbf{N} \right) H_z = \frac{\omega^2}{c^2} H_z \tag{17}$$

wherein $\mathbf{M}$ and $\mathbf{N}$ are $NG \times NG$ matrices:

$$\begin{aligned} \mathbf{M}_{\mathbf{G}_\parallel, \mathbf{G'}_\parallel} &= (1-f)|\mathbf{k}_\parallel + \mathbf{G}_\parallel|^2 \delta(\mathbf{G}_\parallel - \mathbf{G'}_\parallel) - I(\mathbf{G}_\parallel - \mathbf{G'}_\parallel)(\mathbf{k}_\parallel + \mathbf{G}_\parallel) \cdot (\mathbf{k}_\parallel + \mathbf{G'}_\parallel) \\ \mathbf{N}_{\mathbf{G}_\parallel, \mathbf{G'}_\parallel} &= f|\mathbf{k}_\parallel + \mathbf{G}_\parallel|^2 \delta(\mathbf{G}_\parallel - \mathbf{G'}_\parallel) + I(\mathbf{G}_\parallel - \mathbf{G'}_\parallel)(\mathbf{k}_\parallel + \mathbf{G}_\parallel) \cdot (\mathbf{k}_\parallel + \mathbf{G'}_\parallel) \end{aligned} \tag{18}$$

Optics EXPRESS

As in the TM case, identical substitutions are applied to Eq. (17) and the denominator is removed to simplify the expression to:

$$(\theta^5\mathbf{I} + \theta^4\mathbf{S} - \theta^3\mathbf{T} - \theta^2\mathbf{U} + \theta\mathbf{V} + \mathbf{W})H_z = 0 \tag{19}$$

where

$$\begin{aligned}
\mathbf{S} &= i(\mu_a + \mu_b)\mathbf{I} \\
\mathbf{T} &= \mathbf{M} + \mathbf{N} + (\eta_a^2 + \eta_b^2 + \mu_a\mu_b)\mathbf{I} \\
\mathbf{U} &= i(\mu_a + \mu_b)\mathbf{M} + i(\mu_a + \mu_b)\mathbf{N} + i(\mu_b\eta_a^2 + \mu_a\eta_b^2)\mathbf{I} \\
\mathbf{V} &= (\eta_a^2 + \mu_a\mu_b)\mathbf{M} + (\eta_b^2 + \mu_a\mu_b)\mathbf{N} + \eta_a^2\eta_b^2\mathbf{I} \\
\mathbf{W} &= i(\mu_b\eta_a^2 + \mu_a\eta_b^2)\mathbf{I}
\end{aligned} \tag{20}$$

By applying a linear transformation to Eq. (19), the matrix form of the eigenvalue equation for TE wave is derived:

$$\begin{pmatrix} \mathbf{O} & \mathbf{I} & \mathbf{O} & \mathbf{O} & \mathbf{O} \\ \mathbf{O} & \mathbf{O} & \mathbf{I} & \mathbf{O} & \mathbf{O} \\ \mathbf{O} & \mathbf{O} & \mathbf{O} & \mathbf{I} & \mathbf{O} \\ \mathbf{O} & \mathbf{O} & \mathbf{O} & \mathbf{O} & \mathbf{I} \\ -\mathbf{W} & -\mathbf{V} & \mathbf{U} & \mathbf{T} & -\mathbf{S} \end{pmatrix} \begin{pmatrix} H_z \\ \theta H_z \\ \theta^2 H_z \\ \theta^3 H_z \\ \theta^4 H_z \end{pmatrix} = \theta \begin{pmatrix} H_z \\ \theta H_z \\ \theta^2 H_z \\ \theta^3 H_z \\ \theta^4 H_z \end{pmatrix} \tag{21}$$

Upon solving for the eigenvalue θ in Eq. (21), the eigenfrequency is determined using the relation $\omega = \theta c$, thereby enabling the derivation of the band structure for the TE wave in the metallic PC. As with the TM wave, the damping frequency exerts minimal impact on solving eigenvalues. When $\omega_{\tau a} = \omega_{\tau b} = 0$, namely, $\mu_a = \mu_b = 0$, and $\mathbf{S} = \mathbf{U} = \mathbf{W} = \mathbf{O}$, the matrix equation simplifies to:

$$\begin{pmatrix} \mathbf{O} & \mathbf{I} \\ -\mathbf{V} & \mathbf{T} \end{pmatrix} \begin{pmatrix} H_z \\ \theta^2 H_z \end{pmatrix} = \theta^2 \begin{pmatrix} H_z \\ \theta^2 H_z \end{pmatrix} \tag{22}$$

This reduction transforms the operator matrix from $5\,NG \times 5\,NG$ to $2\,NG \times 2\,NG$, leading to an approximately sixfold enhancement in computational efficiency.

If the background material consists of air and the damping frequency is excluded from consideration, substituting $\eta_b = \mu_a = \mu_b = 0$ into Eq. (20) allows for the band structure to be obtained by solving Eq. (22), offering a more concise and clear form compared to Ref. [37]. Note that the eigenvalue of the operator matrix in Eq. (22) is θ^2, and therefore the eigenfrequency $\omega = \sqrt{\theta^2}c$.

2.2. Photonic band characteristics of 2D metallic photonic crystals

To confirm the accuracy of the derived formulas and the implemented algorithms, data from Ref. [37] was utilized to compute the photonic band structure of metallic columns arranged in air ($\omega_{pa} = 2\pi c/a$, $\omega_{\tau a} = 0$, $\omega_{pb} = 0$, $\omega_{\tau b} = 0$). Figures 1 and 2 depict the band structures of square and triangular lattice PCs, respectively (refer to Table 1 for lattice information). All bands were computed with $NG = 441$ plane waves. The obtained results correspond closely with those presented in Ref. [37].

Within the TM band of both square and triangular lattice metallic PCs, distinctive characteristics manifest compared to dielectric PCs. Notably, the lowest frequency in the metallic PC band is consistently greater than zero, forming a bandgap region from zero frequency to a critical cutoff

Optics EXPRESS

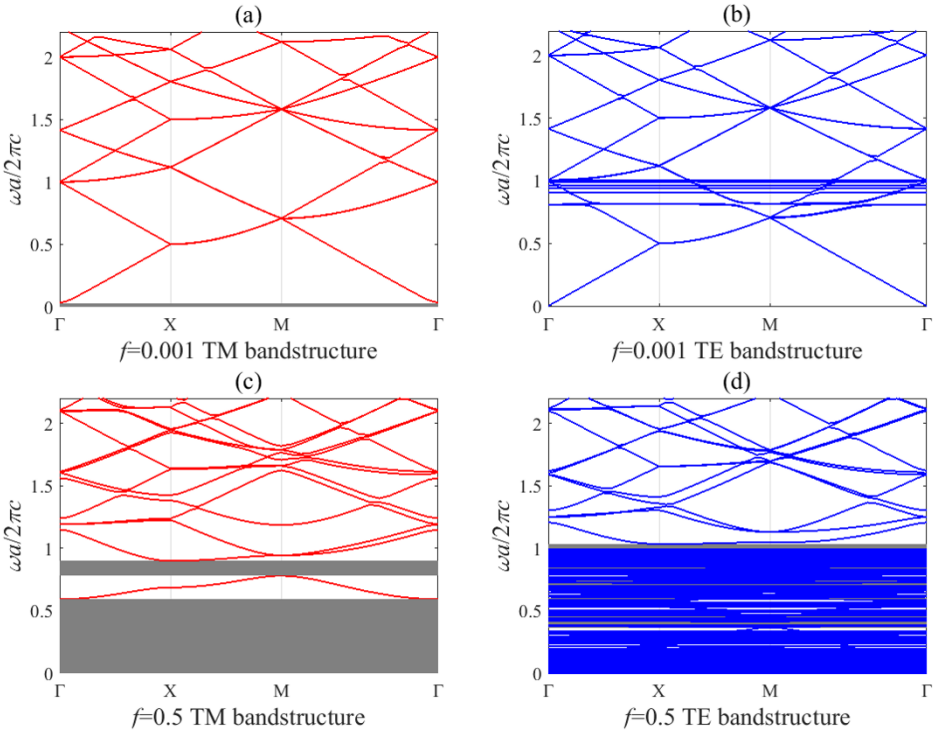

Fig. 1. Band structures of a square lattice metallic photonic crystal. (a) TM band at a filling ratio $f = 0.001$, (b) TE band at $f = 0.001$, (c) TM band at $f = 0.5$, (d) TE band at $f = 0.5$.

frequency [40,41]. As the radius of the metallic column increases, inducing a rise in the filling rate, a metallic wall between adjacent columns obstructs electromagnetic wave propagation, resulting in an increase in the cutoff frequency.

In metallic PCs under TE mode, numerous flat dispersion curves emerge near the band with a normalized frequency of 1, a phenomenon that intensifies as the filling rate increases. This is attributed to the interaction between electromagnetic waves and the metal surface, which generates surface plasma waves propagating along it [42]. As a result, the TE wave's PC band calculations using the PWE method exhibit poor convergence [43]. At higher filling ratios, the emergence of an additional flat curve in the low-frequency band obscures regular band data, rendering the PWE method less effective. In such scenarios, alternative approaches like the Finite Difference Time Domain (FDTD) method become necessary, applying a set threshold to achieve precise photonic band information [39]. Furthermore, when comparing bands calculated through the PWE method to those derived via FDTD, it is evident that PWE achieves rapid convergence for a single unit cell, with the use of 441 plane waves ensuring the desired accuracy in convergence. In this paper, the Lumerical FDTD solutions software is used for FDTD simulations.

Under a specific filling ratio, linear dispersion regions resembling dielectric PCs are observed near K points in the band structure of triangular lattice metallic PCs (indicated by the black arrow in Fig. 2(c)). This region corresponds to the Dirac cone, suggesting the possibility of achieving Dirac frequency localized patterns in metallic PCs, as explored in the next section.

Given that metals are transparent to TE waves, there is an absence of an evident bandgap, Dirac cone, or cutoff frequency comparable to the TM band. Consequently, the focus of the investigation on metallic PCs primarily centers on TM polarization, and therefore, this study will continue to concentrate on TM polarization.

Optics EXPRESS

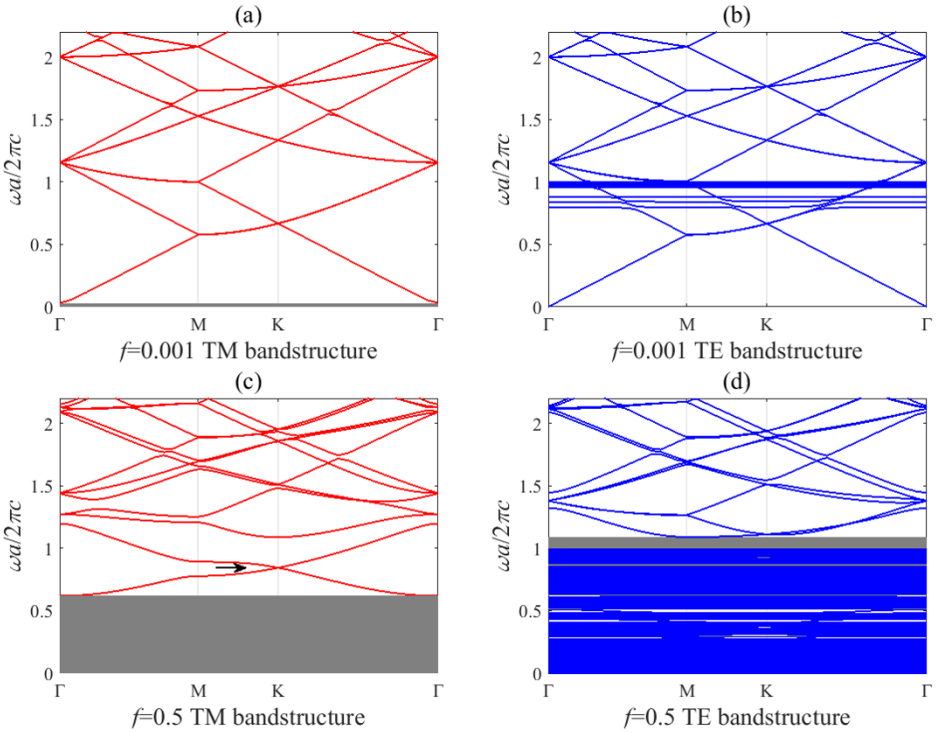

Fig. 2. Band structures of a triangular lattice metallic photonic crystal. (a) TM band at a filling ratio $f = 0.001$, (b) TE band at $f = 0.001$, (c) TM band at $f = 0.5$, (d) TE band at $f = 0.5$.

Furthermore, beyond metallic column PCs arranged in an air background, the introduction of plasma into the background creates 2D plasma background metallic PCs [44]. Taking the triangular lattice as an example, where $\omega_0 = 2\pi c/a$, assume that the metal column has $\omega_{pa} = \omega_0$, $\omega_{\tau a} = 0$, the filling ratio $f = 0.5$, and the plasma frequency of the background is ω_{pb}. Given that the damping frequency exerts minimal influence on the band structure calculation, it can be assumed to be $\omega_{\tau b} = 0.001\omega_0$. Figure 3 shows the band structure diagram including the plasma background. Compared with Fig. 2(c), it can be observed that after plasma filling, the TM dispersion curve significantly rises upward, the cutoff frequency increases, the Dirac point increases, while the width of the Dirac cone decreases. As the plasma frequency increases, the upward trend is notably enhanced. However, when the plasma frequency reaches a certain value,

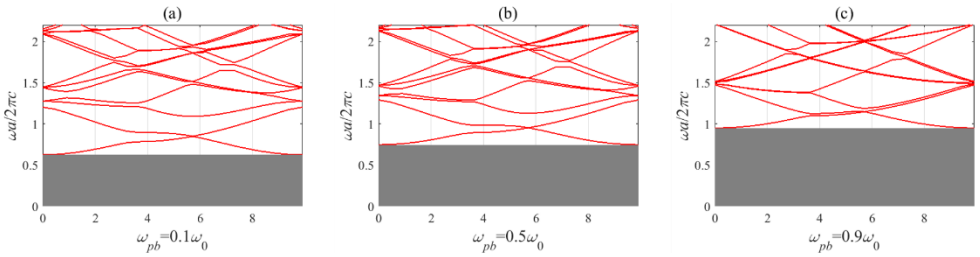

Fig. 3. TM band structures of triangular lattice metallic photonic crystal with plasma backgrounds. (a) Band at $\omega_{pb} = 0.1\omega_0$. (b) Band at $\omega_{pb} = 0.5\omega_0$. (c) Band at $\omega_{pb} = 0.9\omega_0$.

Optics EXPRESS

the Dirac cone is annihilated, and a true Dirac point cannot be formed at this point. Therefore, the introduced plasma can adjust the bandgap and Dirac point position of the metallic PC, and control the formation and closure of the Dirac cone, offering possibilities for creating tunable PC devices.

3. Dirac points in metallic photonic crystals

In Chapter 6.2.4 of Ref. [45], bandgap quantification is elaborated upon using a perturbative formulation rooted in the PWE method. The phenomenon of emerging Dirac cones in PCs comprising dielectric materials polarized by TE is examined in scenarios with minor refractive index differences [21]. Likewise, the linearization PWE method can be utilized to investigate the formation of Dirac cones in metallic PCs via this perturbative approach when polarized by TM. To simplify the analytical model, the focus is narrowed to triangular lattice metallic PCs arranged in air, excluding metal material losses from the analysis. In these crystals with a specified lattice constant a, the dielectric function of the metal is defined as $\varepsilon_a(\omega) = 1 - {\omega_{pa}}^2/\omega^2$, with $\varepsilon_b = 1$ for the air background, the cross-sectional radius of the metallic column being r_a, and the filling ratio indicated as f. Details on the lattice structure diagram, lattice basis vectors, and reciprocal lattice basis vectors are provided in Table 1. Moreover, the first Brillouin zone and six highly symmetric K points are depicted in Fig. 4, featuring wavevectors at these points as $\mathbf{K}_1 = \frac{2\pi}{a}\left(\frac{1}{3}, \frac{\sqrt{3}}{3}\right)$, $\mathbf{K}_2 = \frac{2\pi}{a}\left(-\frac{2}{3}, 0\right)$, $\mathbf{K}_3 = \frac{2\pi}{a}\left(\frac{1}{3}, -\frac{\sqrt{3}}{3}\right)$, $\mathbf{K'}_1 = \frac{2\pi}{a}\left(\frac{2}{3}, 0\right)$, $\mathbf{K'}_2 = \frac{2\pi}{a}\left(-\frac{1}{3}, \frac{\sqrt{3}}{3}\right)$, $\mathbf{K'}_3 = \frac{2\pi}{a}\left(-\frac{1}{3}, -\frac{\sqrt{3}}{3}\right)$, respectively.

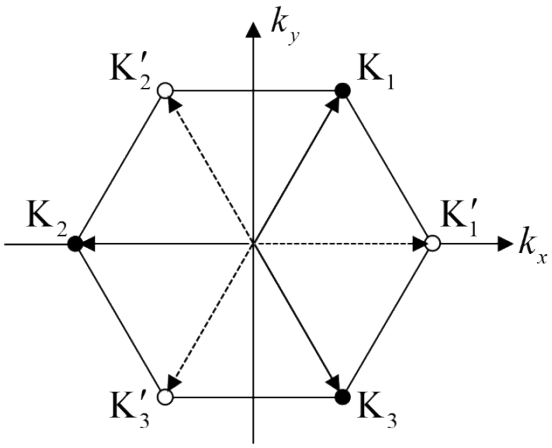

Fig. 4. The first Brillouin zone and six highly symmetric K points of a triangular lattice metallic photonic crystal.

3.1. Split of the triple degenerate eigenstate at K point

Using the improved linearization PWE method, the photonic band structure of the 2D metallic PC TM mode can be calculated using Eq. (14). When $\delta\varepsilon(\omega) = \varepsilon_a(\omega) - \varepsilon_b \to 0$, i.e., ${\omega_{pa}}^2/\omega^2 \to 0$, which is equivalent to the propagation of electromagnetic waves in the air, the band is exactly the same as that of ordinary dielectric PCs, and there is a triple degeneracy at point K_1 [21]. Due to the degeneracy of frequency, the general solution of the electric field expressed by Eq. (7) can

Optics EXPRESS

be simplified to a linear combination containing only three plane waves [21]:

$$E_z(\mathbf{r}) = \sum_{\mathbf{G}\in\{\mathbf{G}_1,\mathbf{G}_2,\mathbf{G}_3\}} E_z^{\mathrm{K}_1}(\mathbf{G})\exp[i(\mathbf{K}_1+\mathbf{G})\cdot\mathbf{r}] \tag{23}$$

where $\mathbf{G}_1 = \frac{2\pi}{a}(0,0)$, $\mathbf{G}_2 = \frac{2\pi}{a}\left(-1,-\frac{\sqrt{3}}{3}\right)$, $\mathbf{G}_3 = \frac{2\pi}{a}\left(0,-\frac{2\sqrt{3}}{3}\right)$, and the wave vector $\mathbf{K}_1+\mathbf{G}$ points to the three corners of the Brillouin zone: $\mathbf{K}_1 = \mathbf{K}_1+\mathbf{G}_1$, $\mathbf{K}_2 = \mathbf{K}_1+\mathbf{G}_2$, $\mathbf{K}_3 = \mathbf{K}_1+\mathbf{G}_3$, so that $|\mathbf{K}_1+\mathbf{G}_{1,2,3}| = 4\pi/(3a) \equiv K$. The triple degeneracy frequency at this situation is $\omega_T = c|\mathbf{K}_1+\mathbf{G}_{1,2,3}| = cK$.

When ${\omega_{pa}}^2/\omega^2 > 0$ and gradually changes, the dielectric PC model is no longer applicable, and the eigenstate needs to be obtained using Eq. (14). By retaining the reciprocal lattice vectors $\mathbf{G} \in \{\mathbf{G}_1, \mathbf{G}_2, \mathbf{G}_3\}$, the eigenequation Eq. (14) can be simplified to:

$$\mathbf{M}_{\mathbf{K}_1}^{\mathrm{TM}} \begin{pmatrix} E_z^{\mathrm{K}_1}(\mathbf{G}_1) \\ E_z^{\mathrm{K}_1}(\mathbf{G}_2) \\ E_z^{\mathrm{K}_1}(\mathbf{G}_3) \end{pmatrix} = 0 \tag{24}$$

where the coefficient matrix $\mathbf{M}_{\mathbf{K}_1}^{\mathrm{TM}}$ is:

$$\mathbf{M}_{\mathbf{K}_1}^{\mathrm{TM}} = \begin{pmatrix} |\mathbf{K}_1+\mathbf{G}_1|^2 + f\frac{\omega_{pa}^2}{c^2} - \frac{\omega^2}{c^2} & \frac{\omega_{pa}^2}{c^2}I(\delta G) & \frac{\omega_{pa}^2}{c^2}I(\delta G) \\ \frac{\omega_{pa}^2}{c^2}I(\delta G) & |\mathbf{K}_1+\mathbf{G}_2|^2 + f\frac{\omega_{pa}^2}{c^2} - \frac{\omega^2}{c^2} & \frac{\omega_{pa}^2}{c^2}I(\delta G) \\ \frac{\omega_{pa}^2}{c^2}I(\delta G) & \frac{\omega_{pa}^2}{c^2}I(\delta G) & |\mathbf{K}_1+\mathbf{G}_3|^2 + f\frac{\omega_{pa}^2}{c^2} - \frac{\omega^2}{c^2} \end{pmatrix} \tag{25}$$

where $\delta G_{ij} = |\mathbf{G}_i - \mathbf{G}_j| = 4\pi/(\sqrt{3}a) \equiv \delta G$. If $\omega_0 = 2\pi c/a$, let $\omega_{pa} = t\omega_0$, then $\delta\varepsilon(\omega) = -t^2{\omega_0}^2/\omega^2$. For ease of calculation, we define:

$$\begin{aligned} \varphi(0) &= |\mathbf{K}_1+\mathbf{G}_i|^2 + f\frac{\omega_{pa}^2}{c^2} = K^2 + ft^2\frac{\omega_0^2}{c^2} \\ \varphi(\delta G) &= \frac{\omega_{pa}^2}{c^2}I(\delta G_{ij}) = t^2\frac{\omega_0^2}{c^2}I(\delta G) \end{aligned} \tag{26}$$

Solve the eigenvalue equation $\det|\mathbf{M}_{\mathbf{K}_1}^{\mathrm{TM}}| = 0$ for TM polarization, where the determinant is:

$$\begin{aligned} \det|\mathbf{M}_{\mathbf{K}_1}^{\mathrm{TM}}| &= \begin{vmatrix} \varphi(0)-\omega^2/c^2 & \varphi(\delta G) & \varphi(\delta G) \\ \varphi(\delta G) & \varphi(0)-\omega^2/c^2 & \varphi(\delta G) \\ \varphi(\delta G) & \varphi(\delta G) & \varphi(0)-\omega^2/c^2 \end{vmatrix} \\ &= [\varphi(0)+2\varphi(\delta G)-\omega^2/c^2][\varphi(0)-\varphi(\delta G)-\omega^2/c^2]^2 \end{aligned} \tag{27}$$

Then the eigenvalues and eigenvectors corresponding to Eq. (27) can be obtained:

$$\begin{aligned} &\left(E_{z1}^{\mathrm{K}_1}(\mathbf{G}_1) \quad E_{z1}^{\mathrm{K}_1}(\mathbf{G}_2) \quad E_{z1}^{\mathrm{K}_1}(\mathbf{G}_3)\right) = \left(1 \quad \eta \quad \eta^*\right), \quad \omega_1^2 = c^2[\varphi(0)-\varphi(\delta G)] = c^2K^2 + t^2\omega_0^2[f - I(\delta G)] \equiv \omega_D^2 \\ &\left(E_{z2}^{\mathrm{K}_1}(\mathbf{G}_1) \quad E_{z2}^{\mathrm{K}_1}(\mathbf{G}_2) \quad E_{z2}^{\mathrm{K}_1}(\mathbf{G}_3)\right) = \left(1 \quad \eta^* \quad \eta\right), \quad \omega_2^2 = c^2[\varphi(0)-\varphi(\delta G)] = c^2K^2 + t^2\omega_0^2[f - I(\delta G)] \equiv \omega_D^2 \\ &\left(E_{z3}^{\mathrm{K}_1}(\mathbf{G}_1) \quad E_{z3}^{\mathrm{K}_1}(\mathbf{G}_2) \quad E_{z3}^{\mathrm{K}_1}(\mathbf{G}_3)\right) = \left(1 \quad 1 \quad 1\right), \quad \omega_3^2 = c^2[\varphi(0)+2\varphi(\delta G)] = c^2K^2 + t^2\omega_0^2[f + 2I(\delta G)] \equiv \omega_S^2 \end{aligned} \tag{28}$$

where $\eta = e^{i2\pi/3}$. Equation (28) reveals that in the TM mode of the triangular lattice metallic PC at the K_1 corner of the first Brillouin zone, the original triple degenerate photonic band will split as t deviates from zero, forming a double degenerate state with an angular frequency ω_D and a

Optics EXPRESS

non-degenerate state with an angular frequency ω_S. By substituting Eq. (28) into Eq. (23), the general solution of the electric field at the K_1 point is:

$$\begin{aligned} E_{z1}^{K_1}(\mathbf{r}) &= (e^{i\mathbf{G}_1\cdot\mathbf{r}} + \eta e^{i\mathbf{G}_2\cdot\mathbf{r}} + \eta^* e^{i\mathbf{G}_3\cdot\mathbf{r}})e^{i\mathbf{K}_1\cdot\mathbf{r}} = e^{i\mathbf{K}_1\cdot\mathbf{r}} + \eta e^{i\mathbf{K}_2\cdot\mathbf{r}} + \eta^* e^{i\mathbf{K}_3\cdot\mathbf{r}} \\ E_{z2}^{K_1}(\mathbf{r}) &= (e^{i\mathbf{G}_1\cdot\mathbf{r}} + \eta^* e^{i\mathbf{G}_2\cdot\mathbf{r}} + \eta e^{i\mathbf{G}_3\cdot\mathbf{r}})e^{i\mathbf{K}_1\cdot\mathbf{r}} = e^{i\mathbf{K}_1\cdot\mathbf{r}} + \eta^* e^{i\mathbf{K}_2\cdot\mathbf{r}} + \eta e^{i\mathbf{K}_3\cdot\mathbf{r}} \\ E_{z3}^{K_1}(\mathbf{r}) &= (e^{i\mathbf{G}_1\cdot\mathbf{r}} + e^{i\mathbf{G}_2\cdot\mathbf{r}} + e^{i\mathbf{G}_3\cdot\mathbf{r}})e^{i\mathbf{K}_1\cdot\mathbf{r}} = e^{i\mathbf{K}_1\cdot\mathbf{r}} + e^{i\mathbf{K}_2\cdot\mathbf{r}} + e^{i\mathbf{K}_3\cdot\mathbf{r}} \end{aligned} \tag{29}$$

The general solutions of the electric field at other K and K' points can be obtained in the same way, following a similar form as Eq. (29). By comparing Eq. (29) with the findings in Ref. [21], it becomes evident that the electric field distribution at the corner of the first Brillouin zone of metallic and dielectric triangular lattice PCs shares a very similar form, differing only in their frequencies. We can draw upon the research methods applied to dielectric PCs to further investigate metallic PCs.

3.2. Linear dispersion at corners of the hexagonal first Brillouin zone

When the Bloch wave vector $\mathbf{k}$ deviates from the Brillouin corner with $\delta\mathbf{k} \equiv \mathbf{k} - \mathbf{K}_1$, the new eigenstate $(\hat{E}_{z1}^{K_1}, \hat{E}_{z2}^{K_1}, \hat{E}_{z3}^{K_1})$ needs to be obtained by solving an eigenequation similar to Eq. (24), where the new coefficient matrix $\mathbf{M}_{\mathbf{k}}^{TM}$ is given by:

$$\mathbf{M}_{\mathbf{k}}^{TM} = \begin{pmatrix} |\mathbf{K}_1 + \delta\mathbf{k}|^2 + f\frac{\omega_{pa}^2}{c^2} - \frac{\omega^2}{c^2} & \frac{\omega_{pa}^2}{c^2} I(\delta G) & \frac{\omega_{pa}^2}{c^2} I(\delta G) \\ \frac{\omega_{pa}^2}{c^2} I(\delta G) & |\mathbf{K}_2 + \delta\mathbf{k}|^2 + f\frac{\omega_{pa}^2}{c^2} - \frac{\omega^2}{c^2} & \frac{\omega_{pa}^2}{c^2} I(\delta G) \\ \frac{\omega_{pa}^2}{c^2} I(\delta G) & \frac{\omega_{pa}^2}{c^2} I(\delta G) & |\mathbf{K}_3 + \delta\mathbf{k}|^2 + f\frac{\omega_{pa}^2}{c^2} - \frac{\omega^2}{c^2} \end{pmatrix} \tag{30}$$

Let $\lambda = \omega^2/c^2$, $d_i = 2\mathbf{K}_i\cdot\delta\mathbf{k} + |\delta\mathbf{k}|^2$, and continue to use the substitutions in Eq. (26). The eigenequation can be simplified to:

$$|\mathbf{M}_{\mathbf{k}}^{TM}| = \begin{vmatrix} \varphi(0) + d_1 - \lambda & \varphi(\delta G) & \varphi(\delta G) \\ \varphi(\delta G) & \varphi(0) + d_2 - \lambda & \varphi(\delta G) \\ \varphi(\delta G) & \varphi(\delta G) & \varphi(0) + d_3 - \lambda \end{vmatrix} = 0 \tag{31}$$

By using the equivalent relations $\mathbf{K}_1 + \mathbf{K}_2 + \mathbf{K}_3 = 0$, $(\mathbf{K}_1\cdot\delta\mathbf{k})(\mathbf{K}_2\cdot\delta\mathbf{k}) + (\mathbf{K}_2\cdot\delta\mathbf{k})(\mathbf{K}_3\cdot\delta\mathbf{k}) + (\mathbf{K}_3\cdot\delta\mathbf{k})(\mathbf{K}_1\cdot\delta\mathbf{k}) = -3K^2|\delta\mathbf{k}|^2/4$, and $(\mathbf{K}_1\cdot\delta\mathbf{k})^2 + (\mathbf{K}_2\cdot\delta\mathbf{k})^2 + (\mathbf{K}_3\cdot\delta\mathbf{k})^2 = 3K^2|\delta\mathbf{k}|^2/2$, the quadratic term of $\delta\mathbf{k}$ is retained, and the higher order terms are omitted. After careful sorting and operations, the following results can be obtained:

$$\begin{aligned} &[\lambda - \varphi(0) - 2\varphi(\delta G)][\lambda - \varphi(0) + \varphi(\delta G)]^2 \\ &= 3|\delta\mathbf{k}|^2\{\varphi^2(0) - \varphi^2(\delta G) + \lambda^2 - 2\varphi(0)\lambda - K^2[\varphi(0) - \lambda]\} \end{aligned} \tag{32}$$

When $\delta\mathbf{k} \to 0$, Eq. (32) can be decomposed into a quadratic equation with one variable $[\lambda - \varphi(0) + \varphi(\delta G)]^2 = 0$ and a linear equation with one variable $\lambda - \varphi(0) - 2\varphi(\delta G) = 0$, corresponding to the solutions $\lambda_{1,2}(0) = \varphi(0) - \varphi(\delta G)$ and $\lambda_3(0) = \varphi(0) + 2\varphi(\delta G)$, respectively. The angular frequency is further obtained by $\omega^2 = \lambda c^2$, and the result obtained is completely consistent with the eigenfrequencies in Eq. (28). When $\delta\mathbf{k}$ deviates from zero, the original quadratic equation $[\lambda$

Optics EXPRESS

$-\varphi(0)+\varphi(\delta G)]^2=0$ is modified to:

$$[\lambda-\varphi(0)+\varphi(\delta G)]^2=3|\delta\mathbf{k}|^2\frac{\varphi^2(0)-\varphi^2(\delta G)+\lambda^2-2\varphi(0)\lambda-K^2[\varphi(0)-\lambda]}{\lambda-\varphi(0)-2\varphi(\delta G)} \tag{33}$$

By approximating the value $\lambda_{1,2}(0)$ to the right end of Eq.(33), $\lambda_{1,2}(\delta\mathbf{k})$ can be obtained by the following equation:

$$\begin{aligned}&[\lambda_{1,2}(\delta\mathbf{k})-\varphi(0)+\varphi(\delta G)]^2\\&\approx 3|\delta\mathbf{k}|^2\frac{\varphi^2(0)-\varphi^2(\delta G)+\lambda_{1,2}^2(0)-2\varphi(0)\lambda_{1,2}(0)-K^2[\varphi(0)-\lambda_{1,2}(0)]}{\lambda_{1,2}(0)-\varphi(0)-2\varphi(\delta G)}\\&=K^2|\delta\mathbf{k}|^2\end{aligned} \tag{34}$$

From Eq. (34), we can get $\lambda_{1,2}(\delta\mathbf{k})-\lambda_{1,2}(0)=\pm K|\delta\mathbf{k}|$, substitute $\lambda=\omega^2/c^2$ into the equation, and use the relation $\omega_{1,2}(\delta\mathbf{k})+\omega_D\approx 2\omega_D$ to get:

$$\omega_{1,2}(\delta\mathbf{k})-\omega_D=\pm v_D|\delta\mathbf{k}| \tag{35}$$

where $v_D=c^2K/(2\omega_D)\approx c/2$.

The linearity of the TM dispersion curve is evident in the vicinity of the double degenerate state at the K_1 point in the Brillouin zone of the triangular lattice metallic PC, mirroring the behavior observed in dielectric PCs. Similarly, by modifying the original linear equation $\lambda-\varphi(0)-2\varphi(\delta G)=0$, a non-degenerate band with the following quadratic dispersion relation can be derived:

$$\omega_3(\delta\mathbf{k})-\omega_S=W_S|\delta\mathbf{k}|^2 \tag{36}$$

where $W_S=(c^2/\omega_S)\{1/2+K^2/[3\varphi(\delta G)]\}|\delta\mathbf{k}|^2$.

In Fig. 5, we illustrate the band splitting near the K point for the case of $a=1$, $r_a=0.35a$, $f=0.444$, and $\omega_{pa}=t\omega_0$. At $t=0$, the band structure of the uniform dielectric air generates triple degenerate states at the K point, as depicted by the blue dotted lines. To slightly distinguish between the three triple degenerate bands, here we actually plot the case of $t=0.1$. When $t>0$ (i.e., $t=0.4$), for these structural parameters, we can observe from Eq. (26) that $\varphi(0)>\varphi(\delta G)>0$, and $\varphi(0)-\varphi(\delta G)>K^2$. In Fig. 5, solid curves describe the dispersion relation calculated using Eq. (14), while red circles represent eigenfrequencies at the K point calculated using perturbation solution Eq. (28). The black dotted lines give the asymptotic line analyzed by Eqs. (35) and (36), showing good agreement with the actual dispersion variations.

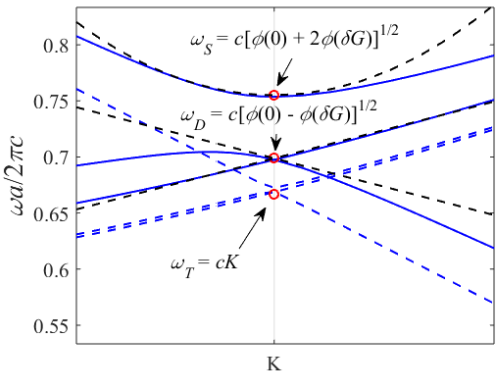

Fig. 5. Splitting of the triple degenerate eigenstate at K.

Optics EXPRESS

As the refractive index contrast increases, the initially triple degenerate state at the Brillouin corner becomes less pronounced, transforming into a double degenerate state at the K_1 point. In the vicinity of this point, the dispersion relation changes linearly. This phenomenon opens up the possibility of creating true Dirac cones in triangular lattice metallic PCs.

4. Localized mode at the Dirac frequency in 2D metallic photonic crystals

4.1. Standing wave solution at the Dirac frequency of metallic photonic crystals

Considering the analogous degeneracies, mode field distribution, and dispersion characteristics shared by the TM mode of the triangular lattice metallic PC at the corner of the first Brillouin zone and its vicinity, in comparison to those of the dielectric PC near the Dirac frequency, we can systematically deduce the cylindrical wave solution for the metallic PC with defects in TM polarization.

To illustrate the viability of an optical bound state at the Dirac frequency within the metallic PC, we delve into the governing equation of the waves in the vicinity of the Dirac frequency. In close proximity to this frequency, photon transport in the transverse plane of the lattice is governed by the massless Dirac equation [13,14]: $-iv_D(\sigma_x\partial/\partial x+\sigma_y\partial/\partial y)\Psi=(\omega-\omega_D)\Psi$. Here, v_D is the group velocity, ω_D is the angular Dirac frequency, σ_x and σ_y are Pauli matrices, and $\Psi=(\psi_1,\psi_2)^{\mathrm{T}}$ represents the envelope amplitudes $\psi_{1,2}$ of a doublet of two degenerate Bloch states at the corners (K points) of the hexagonal first Brillouin zone. In Sec. 3, the general solution of the electric field for the triangular lattice metallic PC at the hexagonal Brillouin corner (K_1 point) is known, as given in Eq. (29). For the Bloch wavevector $\mathbf{k}$ that derivates from K_1 point with $\delta\mathbf{k}\equiv\mathbf{k}-\mathbf{K}_1$, the new wave solution $(\hat{E}_{z1}^{K_1},\hat{E}_{z2}^{K_1},\hat{E}_{z3}^{K_1})$ can be regarded as the original electric field modulated by $\psi_{1,2}$ [13,21], i.e.,

$$\begin{aligned}
\hat{E}_{z1}^{K_1}(\mathbf{r})&\equiv\psi_{1,2}E_{z1}^{K_1}(\mathbf{r})=\psi_{1,2}(e^{i\mathbf{K}_1\cdot\mathbf{r}}+\eta e^{i\mathbf{K}_2\cdot\mathbf{r}}+\eta^* e^{i\mathbf{K}_3\cdot\mathbf{r}})\\
\hat{E}_{z2}^{K_1}(\mathbf{r})&\equiv\psi_{1,2}E_{z2}^{K_1}(\mathbf{r})=\psi_{1,2}(e^{i\mathbf{K}_1\cdot\mathbf{r}}+\eta^* e^{i\mathbf{K}_2\cdot\mathbf{r}}+\eta e^{i\mathbf{K}_3\cdot\mathbf{r}})\\
\hat{E}_{z3}^{K_1}(\mathbf{r})&\equiv\psi_{1,2}E_{z3}^{K_1}(\mathbf{r})=\psi_{1,2}(e^{i\mathbf{K}_1\cdot\mathbf{r}}+e^{i\mathbf{K}_2\cdot\mathbf{r}}+e^{i\mathbf{K}_3\cdot\mathbf{r}})
\end{aligned}\tag{37}$$

The well-established Dirac equation provides a half-bound solution in the form $\psi_{1,2}\propto r^{-m}e^{\mp im\theta}$ at the Dirac frequency. Here r represents the distance between the coordinate point and the original point, θ is the azimuthal angle, and $m=0,\ 1,\ 2\ldots$. This type of mode, previously examined in the context of charge carriers in graphene [7], signifies the probability amplitude of locating spinors in space within the framework of relativistic quantum mechanics. Adapting this relativistic quantum mechanics model for optics involves a slight modification to the interpretation of the modal function. In the domain of PCs, the wave function $\psi_{1,2}\propto r^{-m}e^{\mp im\theta}$ denotes the envelope amplitude of a basis function (Bloch state) [13]. The basis wave function, illustrated in Eq. (29), is intrinsic to a cylindrical geometry and takes the form of a cylindrical wave function [21]: $\phi\propto J_M(Kr)e^{iM\theta}$, where $K=4\pi/(3a)$, M is an integer and $J_M(x)$ is the Mth-order Bessel function.

Consequently, at the Dirac frequency, the physical quantity E_z in the PC is characterized by:

$$E_z\propto r^{-m}J_M(Kr)e^{\pm i(M-m)\theta}\tag{38}$$

In mathematical terms, the first kind of Bessel function is expressed as: $J_M=\frac{1}{2}H_M^{(1)}+\frac{1}{2}H_M^{(2)}$, where $H_M^{(1)}$ and $H_M^{(2)}$ are the first and second kinds of Hankel functions, respectively. These Hankel functions can be written as $H_M^{(1),(2)}=J_M\pm iY_M$, representing forward and backward propagating plane waves, with Y_M being the second kind of Bessel function. Therefore, the electromagnetic wave described by Eq. (38) is not a traveling wave but a standing wave formed by the interference of two counter-propagating cylindrical waves. In standing waves, the phase

Optics EXPRESS

remains constant, with a jump of $\pm\pi$ only at the node. Simultaneously, for large Kr, the Bessel function has an asymptotic form of $J_M(Kr) \approx 2(2\pi Kr)^{-1/2}\cos(Kr - \pi/4 - M\pi/2)$, implying that the amplitude of the Bessel function decays as $r^{-1/2}$. In the cladding region far from the cavity center in the PC resonator, the cylindrical amplitude is proportional to $r^{-m}J_M(Kr)$. Hence, the overall spatial dependence of the corresponding optical state asymptotically approaches $r^{-m-1/2}$ at large distances. This elucidates the emergence of wave localization at the Dirac frequency in such PCs and confirms the algebraic profile of the mode, thereby validating the mathematical model based on the Dirac equation. Such waves cannot exist in an infinitely periodic PC lattice because they are singular at $r = 0$. However, they can exist around a defect in the PC as localized modes. By constructing metallic PC resonators akin to dielectric PCs, we can naturally obtain localized modes at Dirac frequencies.

4.2. Metallic photonic crystal resonant cavity at the Dirac frequency

Similar to the TE mode in dielectric defective PCs [21], we can also construct a TM mode equivalent resonator, as depicted in Fig. 6. To further discuss the electric field solution provided by Eq. (38) for PCs with defects at Dirac frequencies, we equivalently model the metallic PC as a resonant cavity, considering the near-free-photon approximation characterized by low refractive index differences or small defect radii.

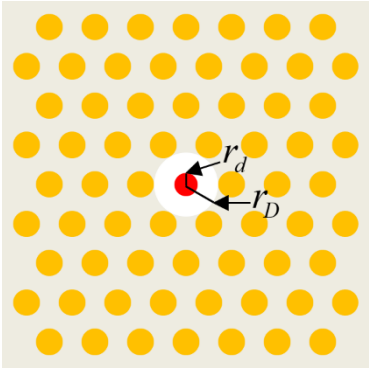

Fig. 6. Resonator model for the triangular lattice metallic photonic crystal.

As shown in Fig. 6, the resonator comprises a defect column represented by a red cylinder (dielectric constant ε_d, radius $r = r_d$), an air ring represented by a white ring (dielectric constant $\varepsilon = 1$, space region $r_d < r \le r_D$), and a PC cladding represented by a light gray region (equivalent dielectric constant ε_2). The yellow cylinders symbolize the metallic columns.

The region of the defect and the surrounding air ring is not a transplantable part of the periodic structure. Nonetheless, as homogeneous materials, the electromagnetic field of the TM mode at this region satisfies the Helmholtz equation in cylindrical coordinates:

$$\left(\frac{\partial^2}{\partial r^2} + \frac{1}{r}\frac{\partial}{\partial r} + \frac{1}{r^2}\frac{\partial^2}{\partial \theta^2}\right) E_z = -\frac{\omega^2}{c^2}\varepsilon_r E_z \tag{39}$$

The solution to the Helmholtz Eq. (39) can be obtained by separating the r and θ variables. Considering the electric field in the cladding represented by Eq. (38), the electric field distribution

Optics EXPRESS

throughout the resonator is given by:

$$E_z = \begin{cases} AJ_N(k_1 r)\exp(iN\theta) & r \le r_d \\ [BJ_N(k_0 r) + CY_N(k_0 r)]\exp(iN\theta) & r_d < r \le r_D \\ Dr^{-m}J_M(Kr)\exp(iN\theta) & r > r_D \end{cases} \tag{40}$$

Here, $N = \pm(M - m)$, $k_0 = \omega/c$, and $k_1 = k_0\sqrt{\varepsilon_d}$. The magnetic field components, H_r and H_θ, are related to the electric field components E_z: $i\omega\mu_0\mu_r H_r = (1/r)\partial E_z/\partial\theta$ and $i\omega\mu_0\mu_r H_\theta = \partial E_z/\partial r$. For non-ferromagnetic materials, $\mu_r \approx 1$, so the magnetic field component is only affected by the partial differential of the electric field and is independent of material properties (dielectric constant or permeability), which is different from the electric field component in the TE mode.

Applying boundary conditions, continuity of the E_z and H_θ components at the interfaces $r = r_d$ and $r = r_D$ yields a system of four coupled equations:

$$\begin{aligned} &AJ_N(k_1 r_d) = BJ_N(k_0 r_d) + CY_N(k_0 r_d) \\ &BJ_N(k_0 r_D) + CY_N(k_0 r_D) = Dr_D^{-m}J_M(Kr_D) \\ &k_1 AJ'_N(k_1 r_d) = k_0 BJ'_N(k_0 r_d) + k_0 CY'_N(k_0 r_d) \\ &k_0 BJ'_N(k_0 r_D) + k_0 CY'_N(k_0 r_D) = Dr_D^{-m}[KJ'_M(Kr_D) - mJ_M(Kr_D)r_D^{-1}] \end{aligned} \tag{41}$$

To facilitate the calculation, define the following variables:

$$\begin{aligned} q &= m - Kr_D\frac{J'_M(Kr_D)}{J_M(Kr_D)} \\ h &= k_0 r_D J'_N(k_0 r_D) + qJ_N(k_0 r_D) \\ g &= k_0 r_D Y'_N(k_0 r_D) + qY_N(k_0 r_D) \end{aligned} \tag{42}$$

If the coefficient matrix of Eq. (41) is denoted as $\mathbf{Q}$, solving the eigenequation $\det|\mathbf{Q}| = 0$ can yield the eigenequation of the TM mode cavity:

$$k_1\frac{J'_N(k_1 r_d)}{J_N(k_1 r_d)} = k_0\frac{hY'_N(k_0 r_d) - gJ'_N(k_0 r_d)}{hY_N(k_0 r_d) - gJ_N(k_0 r_d)} \tag{43}$$

Let $A = 1$ (equivalent to normalizing the peak amplitude of the pattern to 1), and the values of B, C, D can be obtained from the boundary conditions in Eq. (41):

$$\begin{aligned} B &= -\frac{gJ_N(k_1 r_d)}{hY_N(k_0 r_d) - gJ_N(k_0 r_d)} \\ C &= \frac{hJ_N(k_1 r_d)}{hY_N(k_0 r_d) - gJ_N(k_0 r_d)} \\ D &= r_D^m\frac{J_N(k_1 r_d)}{J_M(Kr_D)}\frac{hY_N(k_0 r_D) - gJ_N(k_0 r_D)}{hY_N(k_0 r_d) - gJ_N(k_0 r_d)} \end{aligned} \tag{44}$$

Therefore, the complete electric field distribution expression is:

$$E_z = J_N(k_1 r_d)\exp(iN\theta)\begin{cases} \frac{J_N(k_1 r)}{J_N(k_1 r_d)} & r \leqslant r_d \\ \frac{hY_N(k_0 r) - gJ_N(k_0 r)}{hY_N(k_0 r_d) - gJ_N(k_0 r_d)} & r_d < r \leqslant r_D \\ \frac{r_D^m}{r^m}\frac{J_M(Kr)}{J_M(Kr_D)}\frac{hY_N(k_0 r_D) - gJ_N(k_0 r_D)}{hY_N(k_0 r_d) - gJ_N(k_0 r_d)} & r > r_D \end{cases} \tag{45}$$

By solving the transcendental Eq. (43) for different combinations of m and M values through numerical calculation, the defect parameters ε_d or r_d corresponding to various TM localized

Optics EXPRESS

modes can be obtained. The TM eigenequation does not require an approximation of the effective dielectric constant ε_2 of the cladding region, ensuring higher accuracy than the TE model. The modes predicted by the resonator model can be validated against numerical wave evolution simulations.

We utilize copper as a representative material to validate the localized properties at Dirac frequencies in metallic PCs, employing the PWE method derived in Sec. 2 and the well-established FDTD technique. Figure 7 presents the band information of a triangular lattice copper column PC arranged in air. The lattice constant in this crystal is $a = 1$ μm, and the radius of the copper column is $r_a = 0.25a = 0.25$ μm. Figure 7(a) illustrates the band structure of the PC. Due to the dispersive nature of the medium, we refrain from normalizing the frequency and use actual frequency values. From the figure, we observe a cutoff frequency $f_{cutoff} = 208.93$ THz, two photonic bandgaps in the ranges of $0 \sim f_{cutoff}$ and 355.15 THz ~ 375.41 THz, and two Dirac points at frequencies $f_{d1} = 259.58$ THz and $f_{d2} = 475.56$ THz. Our focus here is solely on the lowest Dirac frequency f_{d1}. To elucidate the shape of the Dirac cones and the variation in the DOS more distinctly, we discretize the Brillouin zone into 100×100 wave vector points. In Fig. 7(b), we present three-dimensional (3D) views of the first and second bands of the crystal, revealing that the two bands touch as a pair of linear Dirac cones at the six corners of the Brillouin zone (depicted by the black hexagon). Simultaneously, the right side of Fig. 7(a) displays the DOS of the eigenmodes counts from these discrete wave vector points. It corresponds one-to-one with the band structure on the left. At the Dirac point f_{d1} marked by the black dashed line, the DOS is zero. Within the range enclosed by the two black solid lines representing the Dirac cones, the DOS exhibits linear variation. The band analysis above further confirms the existence of Dirac cones in metallic PCs, guiding us to continue studying the characteristics of Dirac localized modes.

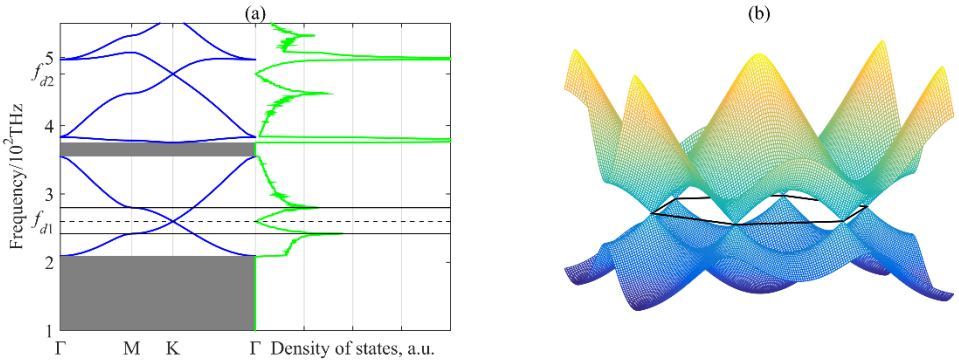

Fig. 7. Band information of a triangular lattice copper column photonic crystal arranged in air with a lattice constant $a = 1$ μm, column radius $r_a = 0.25a = 0.25$ μm, copper dielectric function $\varepsilon_a(\omega) = 1 - {\omega_p}^2/(\omega^2 + i\omega\omega_\tau)$, where $\omega_p = 2\pi \times 1914$ THz, $\omega_\tau = 2\pi \times 8.34$ THz and background dielectric constant $\varepsilon_b = 1$. (a) Band structure (left part) and DOS (right part) of the photonic crystal computed by PWE with $NG = 441$; the black dashed line indicates the Dirac frequency, and the black solid lines represent the range of Dirac cones. (b) 3D view of the first and second bands of the photonic crystal; the black hexagon represents the Brillouin zone.

PC resonant cavities can be realized by introducing a defect through modifying the radius of the central rod or changing its relative permittivity. Here, we maintain the radius of the central metallic column constant ($r_d = r_a$) and replace it with a dielectric cylinder, varying its relative permittivity ε_d, to construct a metallic PC cavity for investigation. The defect modes of the PC cavity can be obtained through a PWE based on a supercell system. However, due to the slow

Optics EXPRESS

convergence rate of the PWE for metallic PCs, making supercell calculations challenging, we employ the well-known FDTD method for the analysis of the metallic PC cavity.

For a metallic PC resonant cavity with a window size of 50 μm × 50 μm, we use spatial steps $\Delta x = a/50$, $\Delta y = \Delta x \cdot \sin(60°)$, and a time step $c\Delta t = 0.6481\Delta x$ to handle a 2D FDTD simulation. To excite the TM modes, we utilize an electric dipole source with a finite lifetime (~ 45 fs) to stimulate wave evolution, ensuring the prompt removal of the external source to allow the dipole to freely radiate. The initial calculation time is maintained at 4000 fs, with adjustments made based on the actual oscillations of the temporal electric field amplitude to ensure sufficient evolution of the electric field. A monitor is placed at the center of the resonant cavity, and the central frequency of the light source and the relative refractive index of the defect are adjusted to observe the frequency domain response at the monitor. Through continuous experimentation and adjustments, we can identify the localized modes of the resonant cavity when its resonance frequency coincides with the center frequency of the narrowband light source.

Figure 8(a) illustrates the frequency of the localized modes in the metallic PC resonant cavity as the relative permittivity of the defect varies. It is observed that localized modes exist in the bandgaps (blue curves) and in the vicinity of the Dirac frequency (red diamonds) when the relative dielectric constant of the defect changes. Specifically, when the dielectric constant of the defect is $\varepsilon_d = 1.80$, the localized mode precisely resonates at the Dirac frequency f_{d1}. The accompanying illustration on the right side depicts the modal field distribution of the electric field $|E_z|$ at the same time. The light blue cylinders symbolize the position of the metallic column, and the wave is confined within the PC. The electric field exhibits a monopole pattern, with the majority of the energy concentrated in the defect rod and its vicinity, representing a typical fundamental mode.

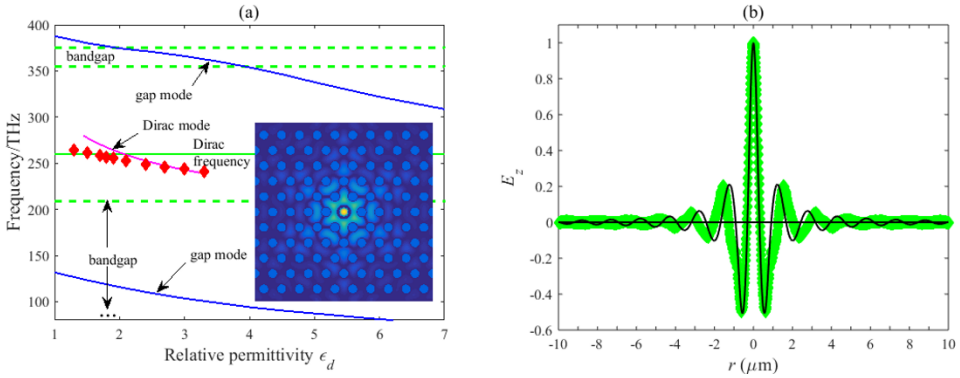

Fig. 8. TM localized modes of a metallic column photonic crystal cavity. (a) Dependence of localized modes as defect relative permittivity changes. Solid green line: Dirac frequency with $f_d = 259.58$ THz. Dashed green lines: edges of the bandgaps. Blue curves: gap modes. Magenta curve: Localized Dirac frequency mode derived from theoretical analysis. Red diamonds: modes calculated from FDTD simulations. Right inset: profile of the fundamental localized mode at the Dirac frequency superimposed on geometric structures of the cavity. (b) Comparison of normalized electric field changes along with distance away from the cavity center between theoretical (solid black line) and FDTD simulations (green points).

The localized modes at the Dirac frequency, obtained through FDTD calculations, are compared with the standing wave solution predicted by Eq. (38). When $m = M = 1$ (N = 0), Eq. (38) precisely represents the TM fundamental mode. By substituting the PC parameters from Fig. 7 into Eq. (43), the defect's relative permittivity corresponding to the fundamental mode around the Dirac frequency is determined. This is shown in the magenta curve of Fig. 8(a), where the defect $\varepsilon_d = 2.08$ precisely matches the Dirac frequency, closely aligning with the defect parameters

Optics EXPRESS

obtained from FDTD calculations. Meanwhile, Fig. 8(b) presents a comparison between the theoretical normalized electric field distribution curve (solid black line), as derived from Eq. (45), and the actual normalized average electric field distribution from FDTD simulations (green points). The two demonstrate excellent concordance, with only minor discrepancies observed at the boundary over the cladding and air ring ($r > 0.75\,\mu$m). This slight variation is deemed acceptable, given that the analytical expression for quasi-plane wave solutions, as outlined in Eq. (37), is primarily applicable near the six corners of the hexagonal first Brillouin zone. In atomic crystal studies, it is a customary approach to represent a discrete system with a continuous approximation, simplifying mathematical analysis. This is done by extending the applicability of Eq. (37) to areas adjacent to the six corners of the hexagonal first Brillouin zone, where the fundamental Dirac mode exhibits rotational symmetry, derived under the continuum limit. Consequently, the C_{6v} discrete rotational symmetry of the numerical solution is approximated by the continuous rotational symmetry of the theoretical outcome. Given the numerical result's dependence on the azimuth angle, an average of the fields in all directions is calculated, represented by green diamonds in Fig. 8(b). This methodological approach yields a good correlation between theoretical predictions and numerical findings.

The existence of the localized cavity mode at the Dirac frequency is due to the disappearance of radiation states at the frequency where DOS is zero. The resonant cavity mode is analyzed exactly at the Dirac frequency, however, in the vicinity of the Dirac frequency, where the DOS is not very large, the loss of radiation states is tolerable. Consequently, a resonant mode similar to that at the Dirac frequency can also be built in this range. As shown in the red diamonds of Fig. 8, the relative permittivity ε_d of the defect rod shifts away from $\varepsilon_d = 1.80$, the resonant frequency of the cavity shifts away from the Dirac frequency. When applied to a resonant frequency ω other than ω_D, we quantitatively require $\delta\omega = |\omega - \omega_D| << \omega_D$ for the result to be valid. In practice, by examining the degree of mode field concentration and the mode decay rate, we typically find it to be accurate within the frequency range of the Dirac cone, and this approach can often be qualitatively extended to even larger frequency ranges.

Figure 9 presents the relevant data obtained from FDTD calculations. The simulated mode profile in Fig. 9(a) provides a 3D representation of the fundamental monopole pattern. In Fig. 9(b), the frequency component $|E_z|$ on the x-axis of the mode is scaled by $r^{3/2}$. The nearly constant oscillation level in the tail of the product indicates a $r^{-3/2}$, asymptotic, algebraic-decay feature of the mode. Because the mode's tail decays faster than $1/r$, the measurable physical quantity $|E_z|$ is square integrable, i.e., $\int |E_z|^2 r dr d\theta < \infty$. The convergence of total energy confirms that this localized mode is a well-behaved, true bound state. Figure 9(c) displays the phase on the mode profile, with the phase undergoing jumps of $\pm\pi$ as the distance changes, indicating a standing wave characteristic. The power-law spatial dependence of the mode in the radial direction and the phase variations are both consistent with Eq. (38) for the case of $m = M = 1$, reaffirming that the new mode is not a traveling wave but a trapped state.

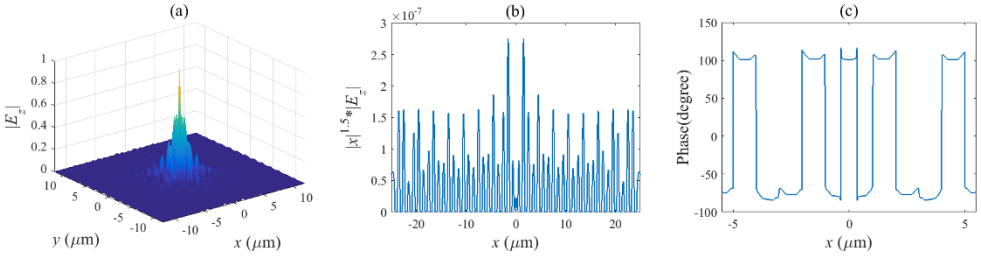

Fig. 9. Properties of the localized mode at the Dirac frequency in a metallic photonic crystal cavity simulated by FDTD. (a) 3D representation of the electric field $|E_z|$, (b) $|x|^{3/2}|E_z|$ variation along the x-axis, (c) phase variation along the x-axis.

Optics EXPRESS

In addition to the fundamental mode, metallic PCs can support various higher-order modes. By substituting different combinations of M and m into Eq. (43), additional sets of defect parameters can be obtained. The FDTD method is employed for a $50\,\mu m \times 50\,\mu m$ cavity to verify these higher-order modes. Table 2 presents three sets of M and m values, along with the corresponding ε_d calculated by solving Eq. (43). Additionally, it provides the step sizes used in FDTD simulations and the resulting defect permittivity under Dirac frequency resonance. Figure 10 illustrates the modal field, decay rate, and phase characteristics of these higher-order modes.

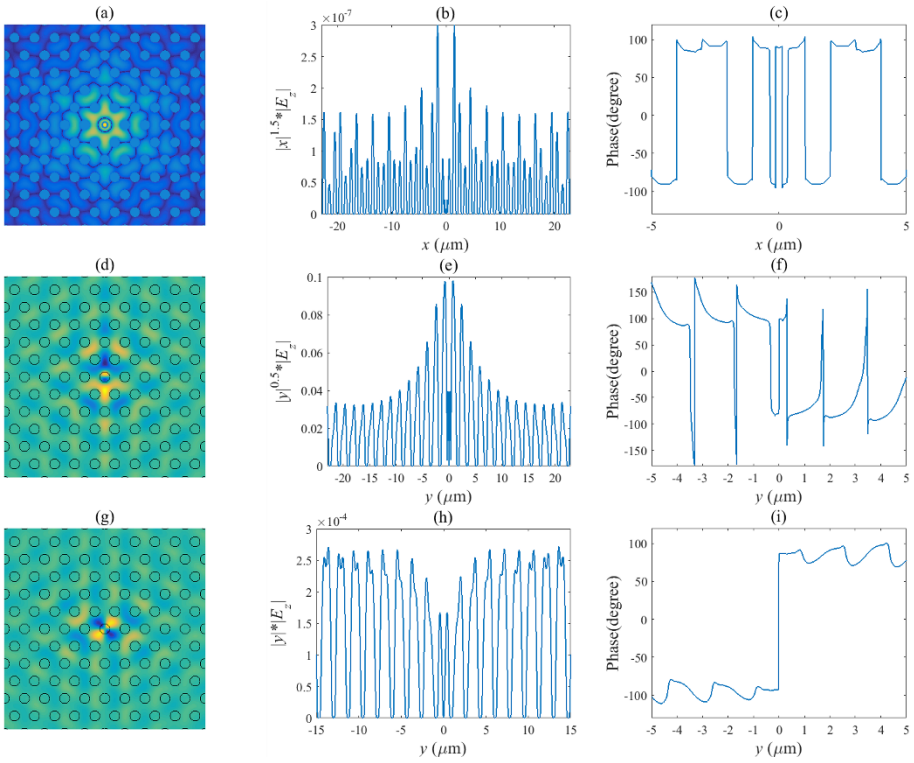

Fig. 10. Higher-order localized modes at the Dirac frequency in a metallic photonic crystal cavity. (a)-(c) Second-order true-bound state for $m = M = 1$: (a) electric field $|E_z|^{1/2}$ pattern profile, with blue rods in the background indicating the positions of cylinder rods, (b) variation of $|x|^{3/2}|E_z|$ on the x-axis, (c) phase variation of the mode on the x-axis. (d)-(f) First ARROW-like mode for $m = 0$, $M = \pm 1$: (d) electric field $\mathrm{Re}[E_z \exp(-i\phi_0)]$, with black circles in the background giving the positions of the rod-air interfaces, (e) variation of $|y|^{1/2}|E_z|$ on the y-axis, (f) phase variation of the mode on the y-axis. (g)-(i) First half-bound mode for $m = -M = 1/2$: (g) electric field $\mathrm{Re}[E_z \exp(-i\phi_0)]$, with black circles in the background indicating the positions of the rod-air interfaces, (h) variation of $|yE_z|$ on the line of $x = 0.36\,\mu m$, (i) phase variation of the mode on the line of $x = 0.36\,\mu m$.

For $m = M = 1$, Eq. (43) has multiple solutions, and Figs. 10(a)-(c) depict a second-order bound state other than the fundamental mode corresponding to Fig. 9. To observe the electric field distribution at non-central positions more clearly, we plot the distribution of $|E_z|^{1/2}$ in Fig. 10(a). It reveals a second-order monopole distribution with an additional nodal plane in the radiative direction. Figure 10(b) demonstrates that the decay rate remains approximately $r^{-3/2}$, and in Fig. 10(c), the phase maintains a jump between $\pm\pi$ and is generally stable.

Optics EXPRESS

Table 2. Higher-order modes of the metallic photonic crystal cavity at Dirac frequency

		ε_d		FDTD step size		
m	M	Theoretical	FDTD	Δx	Δy	$c\Delta t$
1	1	11.82	10.7	a/50	$\Delta x \cdot \sin(60°)$	$0.6481\Delta x$
0	±1	5.71	5.2	a/64	a/80	$0.6184\Delta x$
1/2	−1/2	3.70	5.85	a/64	a/80	$0.6184\Delta x$

When $m = 0$, $M = \pm 1$ ($N = \pm 1$), according to Eq. (38), the corresponding modes exhibit a variation within the PC cladding as $E_z \propto J_1(Kr)e^{\pm i\theta}$ (decaying as $r^{-1/2}$), resembling the Anti-Resonant Reflecting Optical Waveguide (ARROW) mode. Figures 10(d)-(f) represent the first ARROW mode corresponding to Eq. (43). We simulate the excitation of an equal-amplitude clockwise mode ($e^{-i\theta}$) and counterclockwise mode ($e^{i\theta}$) simultaneously using FDTD. As shown in Fig. 10(d), there are two peaks at $(x, y) = (0, \pm 0.15\,\mu\text{m})$, where ϕ_0 is the phase of E_z at the upper peak. The mode pattern resembles an odd-symmetric dipole in the y-direction, and the amplitude curve (Fig. 10(e)) exhibits an algebraic decay law of $r^{-1/2}$ at the mode's end. The phase (Fig. 10(f)) resembles the characteristics of a standing wave.

When m and M are non-integers but satisfy $m - M$ is an integer, i.e., $m = -M = 1/2$ (N = ±(m − M) = ±1), according to Eq. (38), the corresponding mode within the PC cladding will vary as $E_z \propto r^{-1}\cos(Kr)e^{\pm i\theta}$(decaying as $1/r$). Due to the finite decay rate, these modes, classified as half-bound states, do not have square-integrable electric fields. Consequently, the variance between the predicted defect parameter and the numerical outcome is more substantial than in other cases, as detailed in Table 2. Numerical calculations for the first predicted half-bound state are conducted using four radially symmetric source pairs with equal amplitude. The resulting electric field $\text{Re}[E_z\exp(-i\phi_0)]$ at the Dirac frequency is shown in Fig. 10(g), with four peaks located at $(x, y) = (\pm 0.36\,\mu\text{m}, \pm 0.31\,\mu\text{m})$, where ϕ_0 is the phase of E_z at the upper-right peak, and the mode exhibits a central symmetry, as seen in Fig. 10(g). Simultaneous excitation of equal-amplitude clockwise ($e^{-i\theta}$) and counterclockwise ($e^{i\theta}$) modes results in a $\cos\theta$ dependence on the mode's azimuthal angle. The amplitude curve in Fig. 10(h) demonstrates an algebraic decay of $1/r$ at the mode's end, and the phase of the half-bound state in Fig. 10(i) exhibits some fluctuations but is similar to the typical standing wave shape.

Figure 10 displays a mix of bound and half-bound states. The Dirac mode emerges at a conical singularity, characterized by a vanishing density of radiation states. This phenomenon inherently diminishes the coupling between a Dirac mode and radiation states at the Dirac frequency. Therefore, transforming half-bound states into bound states through coherent interference is highly improbable.

4.3. Mode modulation

In our preceding analysis, we explored localized modes at the Dirac frequency within a metallic PC cavity situated in an air background. As depicted in Fig. 3, the introduction of plasmas into the air background allows for the modulation of the Dirac cone's size and the position of the Dirac point. Setting $\omega_{p0} = 2\pi c/a$ (normalized frequency of 1), we fill plasmas ($\omega_{pb} = (0 \sim 1)\omega_{p0}$, $\omega_{\tau b} = 0.002\omega_{p0}$) into the background of the triangular lattice copper column PC shown in Fig. 7. Figure 11(a) presents the variation in relevant band information with the background plasma frequency. In this representation, the dark gray region denotes the photonic bandgap, the upper edge of the lower photonic bandgap (black curve) signifies the cutoff frequency, the light gray region represents the Dirac cone's range, and the internal red curve indicates the Dirac point's position. As ω_{pb}/ω_{p0} varies from $0 \sim 1$, the Dirac point frequency undergoes a corresponding change within the range of approximately 260 THz to 397 THz. With an increase in ω_{pb}, the

Optics EXPRESS

cutoff frequency, Dirac point frequency, and the center of the bandgap all experience a blue shift. By appropriately adjusting the background plasma frequency, we can position the Dirac point at the desired location.

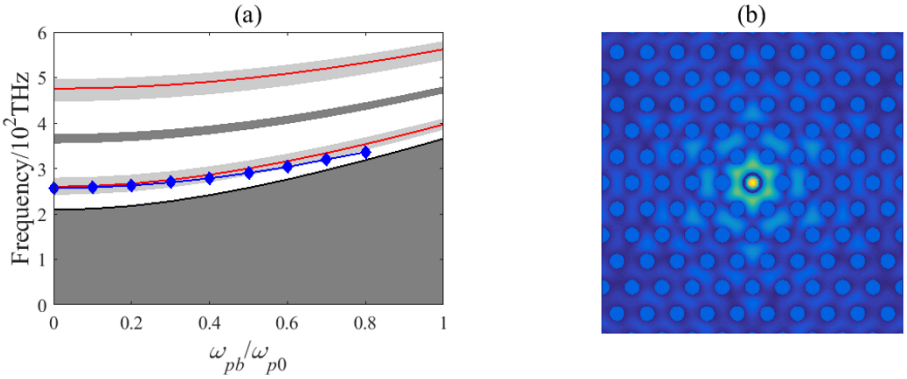

Fig. 11. Modulation of the localized modes in the Dirac cone by the plasma background. (a) Variation of band structure and resonant mode with the background plasma frequency. (b) Resonant mode at $\omega_{pb} = 0.5\omega_{p0}$.

Maintaining the parameters of the metallic PC cavity resonator unchanged, i.e., $r_d = r_a$, $\varepsilon_d = 1.80$, when filling the background with plasmas, the dashed blue diamond line in Fig. 11(a) represents the corresponding variation in the resonance frequency of the cavity. It is observed that when $\omega_{pb}/\omega_{p0} = 0 \sim 0.8$, the resonance frequency of the cavity consistently falls within the range of the Dirac cone. This implies that we can modulate the Dirac localized mode without modifying the defect by simply filling the appropriate plasma background. Figure 11(b) illustrates the schematic of the corresponding resonance mode when $\omega_{pb} = 0.5\omega_{p0}$. Although the resonance frequency does not perfectly coincide with the Dirac point, and there is a slight diffusion in the mode field radius, the mode remains a highly localized fundamental mode. This aligns with the characteristics of the magenta curve and red diamonds representing mode expansion in Fig. 8. In a PC, when the resonant frequency of the cavity generated by the defect deviates from the Dirac frequency, the energy of the localized mode scatters into the continuum states since the DOS of the PC is no longer zero. Consequently, when the resonant frequency of the cavity is non-Dirac, the mode undergoes degeneration, adding a finite bandwidth to the resonance of the cavity for a given structure.

Despite the dispersive nature of metals and the frequency dependence of the dielectric function, we observe that a metallic PC cavity composed of metal medium rods can also support Dirac frequency localized modes, exhibiting properties similar to dielectric PC cavities. Simultaneously, plasma filling holds significant promise for modulating Dirac localized modes in metallic PC cavities, aiding in the generation of Dirac localized modes with extraordinary characteristics in the range of 260 to 336 THz (1327.43 nm ~ 892.86 nm). This insight provides valuable implications for the expanded applications of novel devices.

4.4. *Practical cavity design and experimental validation*

The design of metallic PC cavities resonating at the Dirac frequency mirrors the approach used for conventional PC cavities based on bandgap, albeit with a shift in focus from the bandgap to the Dirac point. Nevertheless, various challenges must be addressed. Firstly, while ideal 2D PCs are theoretically infinite along the z direction, practical constraints necessitate a finite thickness, referred to as PC slabs or planar PCs [46]. Ideally, this thickness should exceed the lattice constant significantly to mitigate disturbances from the slab effect on the Dirac cone [20].

Optics EXPRESS

Additionally, For the TM wave, a PC slab cut off in the z direction by a perfect electrical conductor (PEC) is equivalent to a 2D PC extending indefinitely in the z direction. The PEC, parallel to the equipotential surface of the TM wave, does not affect the electric field orientation of the TM mode but inhibits the appearance of the TE mode. Thus, we can place metallic conductor plates above and below the metallic PC to form a short circuit state, ensuring that only TM modes are excited. Moreover, although ideal PCs extend infinitely in the x and y directions, practical periodic structures terminate at some point, introducing potential edge modes and causing energy leakage. Research has shown [32] that, depending on the specific shape of the PC edge, a defect mode, known as an edge state, may exist at or near the Dirac frequency. However, the presence of edge states depends heavily on the properties of the outermost columns. Special treatments, such as adjusting the refractive index or radius of the outermost column, are necessary to find edge state dispersion curves beneath the light cone. As the dispersion curve of edge states lies beneath the light cone, the wave vector possesses non-radiative characteristics, and excitation of edge states typically requires an internal light source near the edge [32]. Placing the excitation light source close to the central defect further mitigates potential effects of edge states. The finite-sized cavity structure results in mode field leakage when crossing the boundary of the cladding medium. Since the tail of the Dirac mode decays algebraically, stronger than the exponentially decaying tail of the gap mode for the same lattice extent, the Dirac mode generally exhibits higher losses than the gap mode. In the absence of material absorption, the quality factor of the Dirac frequency mode is approximately proportional to the cavity area [21]. Considering the dielectric loss of materials, electric loss weakens the electric field by converting it into thermal energy, affecting the quality factor of the resonant cavity. Generally, metallic materials exhibit higher loss coefficients than dielectric materials. Thus, for resonant cavities requiring a larger quality factor, it is advisable to use metallic materials with lower dielectric losses (such as gold or silver) for periodic structure fabrication. Hence, minimizing the loss due to finite lattice size involves increasing the number of surrounding crystal periods and utilizing metallic materials with low loss factors.

Experimental validation of the localized modes at the Dirac frequency in metallic PCs can be achieved by identifying transmission peaks at various positions within the cavity, as indicated by spectra obtained from the specially designed PC cavity. Additionally, the observation of localized field distribution can be facilitated by capturing images of the mode field. The frequencies associated with the Dirac cone fall within an experimentally accessible range for reasonable values of the cylinder radius (r_a) and lattice constant (a). For example, with $a = 1.4$ μm and $r_a = 0.35$ μm, the Dirac point is located at the wavelength of 1.58 μm, closely matching communication wavelengths. We anticipate that experimental determinations of the localized modes for the systems investigated in this paper will be available in the near future, enabling a comparison with the theoretical results presented here.

5. Conclusion

In summary, this investigation introduces an improved PWE method for calculating the band structure of metallic dispersive PCs with losses, offering versatility across various simplified models, including those without losses or featuring non-dispersive materials. Employing the linearization PWE method, we construct a perturbation approximation and analyze the degeneracy at the Brillouin corners and the dispersion characteristics near these points for TM modes in triangular lattice metallic PCs. Our findings demonstrate the attainment of zero DOS at the K points and the existence of a Dirac cone with linear dispersion and a linearly vanishing DOS in its vicinity within metallic PCs. By introducing the half-bond solution of charge carriers in graphene at the Dirac point and overlaying this relativistic quantum mechanics model onto the envelope amplitude of metallic PC basis wavefunctions, a standing wave solution at the Dirac frequency for defective triangular lattice metallic PCs under TM polarization is derived. This localized mode exists beyond any photonic bandgaps, displaying unconventional algebraic decay

Optics EXPRESS

rates and representing a novel mechanism for metallic PC optical localization. Validation of theoretical results through numerical simulations demonstrates excellent agreement between theory and simulation. Introducing plasma into the background of metallic column PCs allows modulation of the Dirac point's position and the width of the Dirac cone. With a finite bandwidth of the Dirac localized mode, frequency-tunable Dirac localized modes can be achieved under specific resonant cavity parameters. This not only aids in a deeper understanding of the Dirac properties in graphene electronic crystals but also provides robust support for the development of novel micro-nano-photonic integrated devices requiring long-range coupling. Simultaneously, the theoretical analysis of the 2D model lays the groundwork for exploring more practically valuable models such as PC slabs and PC fibers. The study of waves in visible and near-infrared range guides further analysis of microwave-related properties in metallic PCs. Given the role of plasmas as metamaterials in the microwave region, we anticipate that this exploration will broaden the application possibilities of Dirac modes across a range of metamaterial PC devices.

Funding. National Natural Science Foundation of China (11874012, 12174002, 52205548); Excellent Scientific Research and Innovation Team of Anhui Province (2022AH010003); Anhui Provincial Key Research and Development Plan (202104a05020059); Innovation Project for the Returned Overseas Scholars of Anhui Province (2021LCX011); The University Synergy Innovation Program of Anhui Province (GXXT-2020-052); Anhui Young Wanjiang Scholars Talent Project (Z010118167); Postdoctoral Fellowship Program (Grade C) of China Postdoctoral Science Foundation (GZC20230007).

Disclosures. The authors declare that ChatGPT 3.5 was used to polish the language in the writing process while no contents were added from this or any other artificial intelligence tools. The authors declare no other conflicts of interest.

Data availability. Data underlying the results presented in this paper are not publicly available at this time but may be obtained from the authors upon reasonable request.

References

1. K. S. Novoselov, A. K. Geim, S. V. Morozov, *et al.*, "Electric field effect in atomically thin carbon films," Science **306**(5696), 666–669 (2004).
2. A. K. Geim and K. S. Novoselov, "The rise of graphene," Nat. Mater. **6**(3), 183–191 (2007).
3. M. Z. Hasan and C. L. Kane, "Colloquium: Topological insulators," Rev. Mod. Phys. **82**(4), 3045–3067 (2010).
4. K. S. Novoselov, A. K. Geim, S. V. Morozov, *et al.*, "Two-dimensional gas of massless Dirac fermions in graphene," Nature **438**(7065), 197–200 (2005).
5. Y. B. Zhang, Y. -W. Tan, H. L. Stormer, *et al.*, "Experimental observation of the quantum Hall effect and Berry's phase in graphene," Nature **438**(7065), 201–204 (2005).
6. J. Wang, S. Deng, Z. Liu, *et al.*, "The rare two-dimensional materials with Dirac cones," Natl. Sci. Rev. **2**(1), 22–39 (2015).
7. A. H. Castro Neto, F. Guinea, N. M. R. Peres, *et al.*, "The electronic properties of graphene," Rev. Mod. Phys. **81**(1), 109–162 (2009).
8. B. Wunsch, F. Guinea, F. Sols, *et al.*, "Dirac-point engineering and topological phase transitions in honeycomb optical lattices," New J. Phys. **10**(10), 103027 (2008).
9. M. Diem, T. Koschny, C.M. Soukoulis, *et al.*, "Transmission in the vicinity of the Dirac point in hexagonal photonic crystals," Physica B **405**(14), 2990–2995 (2010).
10. H. M. Guo and M. Franz, "Topological insulator on the kagome lattice," Phys. Rev. B **80**(11), 113102 (2009).
11. K. M. Ho, C. T. Chan, C. M. Soukoulis, *et al.*, "Existence of a photonic gap in periodic dielectric structures," Phys. Rev. Lett. **65**(25), 3152–3155 (1990).
12. F. D. M. Haldane and S. Raghu, "Possible realization of directional optical waveguides in photonic crystals with broken time-reversal symmetry," Phys. Rev. Lett. **100**(1), 013904 (2008).
13. S. Raghu and F. D. M. Haldane, "Analogs of quantum-Hall-effect edge states in photonic crystals," Phys. Rev. A **78**(3), 033834 (2008).
14. R. A. Sepkhanov, Y. B. Bazaliy, C. W. J. Beenakker, *et al.*, "Extremal transmission at the Dirac point of a photonic band structure," Phys. Rev. A **75**(6), 063813 (2007).
15. J. Mei, Y. Wu, C. T. Chan, *et al.*, "First-principles study of Dirac and Dirac-like cones in phononic and photonic crystals," Phys. Rev. B **86**(3), 035141 (2012).
16. Z. Wang, Y. D. Chong, J. D. Joannopoulos, *et al.*, "Reflection-free one-way edge modes in a gyromagnetic photonic crystal," Phys. Rev. Lett. **100**(1), 013905 (2008).
17. S. Longhi, "Quantum-optical analogies using photonic structures," Laser Photonics Rev. **3**(3), 243–261 (2009).
18. X. Zhang, "Observing zitterbewegung for photons near the dirac point of a two-dimensional photonic crystal," Phys. Rev. Lett. **100**(11), 113903 (2008).
19. M. Bellec, U. Kuhl, G. Montambaux, *et al.*, "Tight-binding couplings in microwave artificial graphene," Phys. Rev. B **88**(11), 115437 (2013).

Optics EXPRESS

20. S. R. Zandbergen and M. J. A. de Dood, "Experimental Observation of Strong Edge Effects on the Pseudodiffusive Transport of Light in Photonic Graphene," Phys. Rev. Lett. **104**(4), 043903 (2010).
21. K. Xie, H. Jiang, A. D. Boardman, *et al.*, "Trapped photons at a Dirac point: a new horizon for photonic crystals," Laser Photonics Rev. **8**(4), 583–589 (2014).
22. Q. Mao, K. Xie, L. Hu, *et al.*, "Light confinement at a Dirac point in honeycomb-like lattice photonic crystal," Opt. Commun. **384**, 11–15 (2017).
23. Q. Mao, L. Hu, G. Ding, *et al.*, "Observation of the Dirac mode guidance in Kagome lattice of photonic crystals," Opt. Commun. **503**, 127449 (2022).
24. K. Xie, A. D. Boardman, Q. Li, *et al.*, "Spatial algebraic solitons at the Dirac point in optically induced nonlinear photonic lattices," Opt. Express **25**(24), 30349–30364 (2017).
25. K. Xie, W. Zhang, A. D. Boardman, *et al.*, "Fiber guiding at the Dirac frequency beyond photonic bandgaps," Light-Sci. Appl. **4**, 1 (2015).
26. L. Hu, K. Xie, Z. Hu, *et al.*, "Experimental observation of wave localization at the Dirac frequency in a two-dimensional photonic crystal microcavity," Opt. Express **26**(7), 8213–8223 (2018).
27. K. Wang, "Abnormal *K*-point dependent electromagnetic beam propagation in a graphenelike triangular metallic photonic structure," Phys. Rev. B **100**(11), 115140 (2019).
28. K. Wang, "Narrow electromagnetic beam transmission associated to the Dirac cones in a graphenelike photonic crystal," Phys. Rev. B **103**(23), 235107 (2021).
29. W. Zhang, X. Zhang, J. Che, *et al.*, "Properties of eigenmodes and quantum-chaotic scattering in a superconducting microwave Dirac billiard with threefold rotational symmetry," Phys. Rev. B **107**(14), 144308 (2023).
30. W. Zhang and B. Dietz, "Microwave photonic crystals, graphene, and honeycomb-kagome billiards with threefold symmetry: Comparison with nonrelativistic and relativistic quantum billiards," Phys. Rev. B **104**(6), 064310 (2021).
31. S. Bittner, B. Dietz, M. Miski-Oglu, *et al.*, "Observation of a Dirac point in microwave experiments with a photonic crystal modeling graphene," Phys. Rev. B **82**(1), 014301 (2010).
32. S. Bittner, B. Dietz, M. Miski-Oglu, *et al.*, "Extremal transmission through a microwave photonic crystal and the observation of edge states in a rectangular Dirac billiard," Phys. Rev. B **85**(6), 064301 (2012).
33. A. Rashidnia, H. Pakarzadeh, M. Hatami, *et al.*, "Photonic crystal-based biosensor for detection of human red blood cells parasitized by plasmodium falciparum," Opt. Quantum Electron. **54**(1), 38 (2022).
34. Y. Chen, H. Chen, G. Cai, *et al.*, "High transmission in a metal-based photonic crystal," Appl. Phys. Lett. **112**(1), 5 (2018).
35. J. Boehm, M. Bellec, F. Mortessagne, *et al.*, "Microwave Experiments Simulating Quantum Search and Directed Transport in Artificial Graphene," Phys. Rev. Lett. **114**(11), 110501 (2015).
36. Plihal and Maradudin, "Photonic band structure of two-dimensional systems: The triangular lattice," Phys. Rev. B **44**(16), 8565–8571 (1991).
37. V. Kuzmiak, A. A. Maradudin, F. Pincemin, *et al.*, "Photonic band structures of two-dimensional systems containing metallic components," Phys. Rev. B **50**(23), 16835–16844 (1994).
38. M. A. Ordal, L. L. Long, R. J. Bell, *et al.*, "Optical properties of the metals Al, Co, Cu, Au, Fe, Pb, Ni, Pd, Pt, Ag, Ti, and W in the infrared and far infrared," Appl. Opt. **22**(7), 1099 (1983).
39. K. Sakoda, N. Kawai, T. Ito, *et al.*, "Photonic bands of metallic systems. I. Principle of calculation and accuracy," Phys. Rev. B: Condens. Matter Mater. Phys. **64**(4), 045116 (2001).
40. I. El-Kady, M. M. Sigalas, R. Biswas, *et al.*, "Metallic photonic crystals at optical wavelengths," Phys. Rev. B **62**(23), 15299–15302 (2000).
41. A. Kaso and S. John, "Nonlinear Bloch waves in metallic photonic band-gap filaments," Phys. Rev. A **76**(5), 053838 (2007).
42. S. Brand, R. A. Abram, M. A. Kaliteevski, *et al.*, "Complex photonic band structure and effective plasma frequency of a two-dimensional array of metal rods," Phys. Rev. B **75**(3), 035102 (2007).
43. H. Takeda, T. Takashima, K. Yoshino, *et al.*, "Flat photonic bands in two-dimensional photonic crystals with kagome lattices," J. Phys.: Condens. Matter **16**(34), 6317–6324 (2004).
44. T. Fu, Z. Yang, Z. Shi, *et al.*, "Dispersion properties of a 2D magnetized plasma metallic photonic crystal," Phys. Plasma **20**(2), 1 (2013).
45. M. Skorobogatiy and J. Yang, *Fundamentals of Photonic Crystal Guiding* (Cambridge University Press, 2009), pp. 138–142.
46. O. Painter, J. Vučkovič, A. Scherer, *et al.*, "Defect modes of a two-dimensional photonic crystal in an optically thin dielectric slab," J. Opt. Soc. Am. B **16**(2), 275–285 (1999).